The Hydrodynamic & Structural Design of Static Hydrofoils for an Electric Ferry Model

Auteur : Giovinazzi, Riccardo
Promoteur(s) : Rigo, Philippe
Faculté : Faculté des Sciences appliquées
Diplôme : Master : ingénieur civil mécanicien, à finalité spécialisée en "Advanced Ship Design"
Année académique : 2023-2024
URI/URL : http://hdl.handle.net/2268.2/22252







With the support of the Erasmus+ Programme of the European Union

Master Thesis

Presented in partial fulfillment of the requirements for the double degree:

Erasmus Mundus Master Program EMSHIP+

Master of Sciences in Applied Mechanics, Naval Architecture and Advanced Ship Design, conferred by the University of Liege, with a second year specialisation in Hydrodynamics for Ocean Engineering (Master HOE) conferred by the Ecole Centrale de Nantes.

The Hydrodynamic & Structural design of static Hydrofoils for an Electric Ferry Model

Candidate:
Riccardo GIOVINAZZI

Supervisor:
Giles BARKLEY

Academic year 2023-2024

DECLARATION OF AUTHORSHIP

I declare that this thesis and the work presented in it are my own and have been generated by me as the result of my own original research.

Where I have consulted the published work of others, this is always clearly attributed.

Where I have quoted from the work of others, the source is always given. With the exception of such quotations, this thesis is entirely my own work.

I have acknowledged all main sources of help.

Where the thesis is based on work done by myself jointly with others, I have made clear exactly what was done by others and what I have contributed myself.

This thesis contains no material that has been submitted previously, in whole or in part, for the award of any other academic degree or diploma.

I cede copyright of the thesis in favour of Solent University.

Contents

List of Figures

List of Tables

1 Abstract

In order to face the climate hazard that is currently threatening our society and reach the net zero carbon target that the EU government hopes to reach by 2050 through the European Green Deal (Fetting, 2020), new means of green transport must be conceived. This thesis enters the debate on new green solutions by moving away from conventional fossil fuel displacement vessels and proposing a green means of transport: a hydrofoiling trimaran. The vessel is a 66 feet (approximately 20 meters), electric hydrofoiling and high speed ferry, capable of carrying up to 40 passengers on short to medium range coastal routes. The low drag vessel will be accompanied by low power electric motors, which, if used, can be a stepping stone towards reaching the required net zero carbon target. The concept proposed here is developed along the City of Southampton - Isle of Wight route, which is currently serviced by some dilapidated diesel powered traditional ferries. Importantly, however, any other route could have been used to size the vessel.

To simplify the project and allow the build of a trial vessel - which is essential for proving the viability of the concept - the thesis presents the design of a 9 meter demonstrator vessel, smaller than the full-size 66 feet boat. The model vessel is designed in order to test the viability of solutions that are potentially applicable to the full size; for this reason, only those design features applicable to the full-size ferry are included in this smaller version. This thesis thus develops the concept and the studies necessary to adopt the 9 meter demonstrator vessel and recommends iterations of the design loop which can improve its design.

Hereby are the model scale dimensions of the vessel which will be used to size the hydrofoil system.

LOA	8960	mm
BOA	3477	mm
Draft	422	mm
Displacement	1950	kg

Table 1: Model size characteristics

Designing the hull and superstructure of the vessel, however, is beyond the scope of this present work, thus such data is taken from the work of professor Giles Barkley, the supervisor of the thesis. It is due to this engaging supervision and my attendance of the Yacht Design courses at the Solent University, in fact, that Southampton is used as this contribution's case study.

2 Introduction

Hydrofoil technology has evolved significantly since its inception, beginning with the early designs of fixed wing, surface piercing foils to the sophisticated, sensor driven systems seen today (Acosta, 1973). The initial fixed-wing hydrofoils, which emerged in the early 20^{th} century, were characterized by their simple but robust construction, providing lift and reducing hull drag through the water (although the hull was only partially lifted from the free surface). These early models were revolutionary for their time, providing a fairly stable configuration. Yet, they have significant limitations, especially in today's context. They are big, bulky, and very wide, making them prone to hitting objects in the water and difficult to manoeuvre in small ports. Additionally, these hydrofoils are less efficient across various conditions, as they do not have adapting lifting surfaces such as flaps.

In contrast, modern hydrofoils have seen a dramatic transformation, thanks to advances in materials science, hydrodynamics, and control systems. Today's state of the art hydrofoils are equipped with a myriad of sensors and advanced control mechanisms that actively manage wing flaps and adjust angles of attack in real time, ensuring optimal lift and stability, as well as much higher levels of safety on board, guaranteeing efficiency and functionality for any change in speed, load or wave condition (McConaghy Boats et al., 2022). The efficiency gains translate into lower energy consumption and faster travel speeds, which are critical to achieve high speed maritime transportation in terms of a greener solutions. Examples of such modern engine powered vessels include the 37^{th} edition of the Americas Cup chase boats (The Royal New Zealand Yacht Squadron Incorporated et al., 2021), Candela's motorboat range (Candela, 2024) or Artemis's foiling commercial boats (Artemis Technologies, 2022). These vessels have sensors which collect data up to 100 times per second and can move each control surface with a high frequency.

However, the complexity of modern hydrofoils introduces new challenges. The reliance on numerous sensors and control surfaces means that these systems are prone to technical failures, which, if unforeseen, could compromise stability and safety, and lead to the disruption of service in commercial scenarios. The need for advanced electronic and mechanical systems also means that they are expensive to produce and maintain, aspects which require a highly specialized workforce.

Currently, there are no specific regulations which aim to govern the design and operation of hydrofoils (The first regulatory discussions happened at the first World Foiling Congress in Genoa on April 17^{th} 2024). Without standardized guidelines, a lot of safety, reliability, and performance in hydrofoil vessels rely heavily on engineering judgment and the application of best practices, which can result in a unique challenge for engineers or designers working with this technology. The more common hydrofoil technology becomes, the more likely it is that specific rules will be developed by regulatory bodies in the future.

This thesis aims to prove that new solutions, which are different to current models in the

market and which also respond to a series of challenges, can be created. As such, this thesis seeks to propose a new model and, by doing so, propose a solution to the existing limitations that these designs inevitably produce.

3 Hydrofoil design requirements

To overcome the limitations that were presented above, the proposed concept cuts down to the bone all the complex engineering equipment necessary to fly, especially if placed under water. Thus, the proposed model relies on a fully submerged static wing, seemingly similar to the modern hydrofoils yet stripped of its complex systems. This concept also has the additional benefit of reducing maintenance workload and costs, which can value the ferries' service and deal with the lack of highly-skilled operational labour.

3.1 Fixed wing implications

A fixed main wing is only suitable with a small velocity window, which can allow the vessel to work. In a commercial ferry, this is possible since the navigation time and electrical energy needed to complete operations is optimized, hence the vessel will mostly operate at cruise speed. Additionally, the lift-off condition is a key condition for allowing the vessel's entrance into foiling mode, without which the vessel cannot *de facto* foil. On the other hand, inside slow speed zones such as ports or channels, or while performing very small radius turns, the ferry can operate in a full displacement mode. Only in rare occasions will the vessel need to operate at maximum speed, reason why priority is given to the lift-off and cruise speeds.

Although the hydrofoil is sized primarily on a straight line course, also the vessel's turning abilities will be addressed. When turning, the flow of water reaching the structure will be at an angle with respect to the heading of the boat; hence, it is important to address the effect of this angle on the foil system.

3.2 Foil layout

As presented in Figure 1, the foil assembly is composed of a main foil and a rudder foil, both of which are made up of vertical and horizontal elements. The first is comprised of a horizontal central wing capable of creating most of the vertical lift, and necessary for counterbalancing the weight of the boat lifting the hull out of the water. Lateral winglets are placed at the extremities of the central foil in order to improve stability during flight. The main foil assembly is thus supported by two vertical struts, which transfer the load from the wing to the vessel, stressing the elements mostly in compression. The vertical masts must have an aerodynamic shape in order to minimize drag, yet they can create lift when the vessel is turning. The airfoil shape selection process is addressed in Chapter 9. The additional effect of vertical struts is of

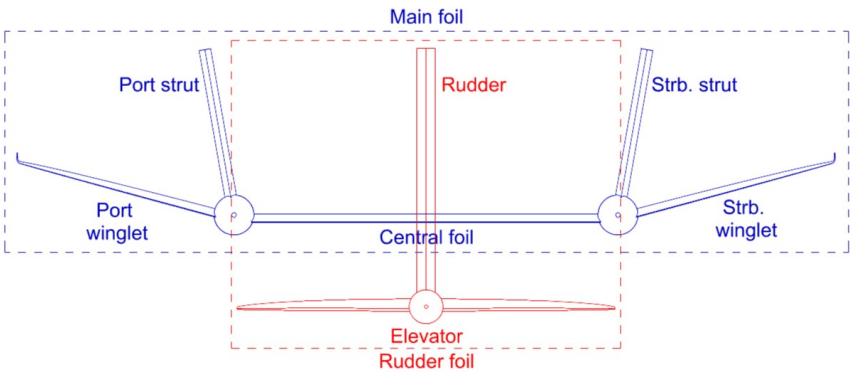

Figure 1: Foil layout

acting as end plates on the central foil, impeding flow slippage from the high to low pressure zones and ensuring that the flow along the span of the main foil is constant; thus improving efficiency.

The rudder is composed of a vertical section - necessary to modify the heading of the vessel - and a horizontal section - defined as elevator -. Submerged moving parts are reduced also on this element, reason why the vertical and horizontal rudder elements are relatively fixed to one another, thus the entire rudder is placed on a double axis hinge. These hinges allow the assembly to move around both the vertical and the transversal axis, enhancing the vessel's control in both yaw and pitch. By modifying the elevator angle, the trim of the vessel is modified (hence also the main foil angle of attack since the foil is fixed), an aspect which varies the forces produced by the wing. Importantly, this is the main parameter influencing the flight control PID loop. Due to the large inertia of the vessel, the wing's response to the need for more (or less) lift is rather slow; yet it can be speeded up by dynamically modifying the wing section with flaps. However, this latter solution is in contrast with this project's objective of removing all the submerged moving parts. Furthermore, ensuring the most optimal safety conditions implies that it is best to have a rudder, which is deeper into the water than the main foil: this guarantees a substantial control over the heading of the vessel even if the main foil happens to leap out of the water.

3.3 PID loop for the control system

By analysing the details of the control system requirements, the PID loop must exploit all the available control methods simultaneously in order to maintain a stable and level flight. As most of the lift generated by the vessel is produced by a fixed submerged wing, the method for increasing or reducing the sink of the vessel is that of varying the global trim angle: the larger the trim angle, the more lift is produced and the more the sink is reduced. Conversely, as the lift produced by the main foil is reduced, the sink is increased. Sink must be always confined between a maximum value (when the vessel is in displacement mode) and a minimum value (when cavitation on the main foil is about to occur). Sink values can be equal to any value

within the two limits, which pilots can set according to the sea state or to broader sailing conditions. In turn, therefore, the trim angle is controlled by both the elevator angle and the throttle input. Considering these aspects, it is clear that the PID loop can control the desired sink by modifying the above-mentioned inputs. For safety reasons, trim values must be confined between an upper and lower limit, as this allows to prevent the main foil from stalling or producing a negative lift. Additionally, as the displacement of the vessel varies, for example with more passengers on board, the required lift is adjusted within the PID loop by changing the target trim of the vessel.

To initiate a vessel's turn, the control system must distinguish the pilot's intended change in heading from the actual rudder position adjustment. The pilot can thus adjust the steering wheel to set the desired rate of heading change (the first derivative of yaw motion), prompting the rudder to reposition accordingly to achieve the target rate of heading change. Since the rudder is expected to create additional unwanted moments, the change in rudder position must be mitigated by the PID loop to maintain safe heel, trim and sink values. In this way, the rudder has a lower priority compared to the just mentioned quantities, and flight control is always guaranteed. If the heading of the vessel must be changed at any cost, for example due to a sudden potential collision, the pilot can press a button which will trigger the sink to its maximum value, allowing the vessel to quickly enter displacement mode, ensuring that a large rudder angle can be easily and quickly applied without the risk of capsizing. The same *rationale* can be applied to the case of the throttle input: after the pilot has set a desired target speed, the PID loop must assign the appropriate power to each motor and thus allow to reach the desired speed, maintaining heel, sink and trim values confined into the desired region. If the vessel cannot maintain adequately safe attitudes, the target speed is not reached in reality. Rolling abilities of the vessel can be further improved by controlling the port and starboard throttle inputs, separately creating an unbalance in thrust force between the two sides of the vessel.

3.4 Full scale and model scale similitude

In order to achieve a 20 knot lift-off speed on the 66 feet full size vessel, the model's target lift-off speed must be equal to 13 knots. This is calculated by means of the Froude similitude at model and full scale:

$$Fr_m = \frac{u_m}{\sqrt{g \cdot L_m}} = \frac{u_f}{\sqrt{g \cdot L_f}} = Fr_f \tag{1}$$

A summary of the cruise speed, lift off speed and maximum speed is found in Table 2.

	Model scale	Full scale
Take-off speed	11 Kn	16 Kn
Cruise speed	13 Kn	19 Kn
Maximum speed	15 Kn	22 Kn

Table 2: Summary of take-off, cruise and max speed at model and full scale

To ensure an effective ferry design, it is essential to prioritize both safety and comfort at all times, minimizing any potential hazards. This requires controlling accelerations and maintaining angular attitudes within acceptable and comfortable limits. A key action for this is preventing cavitation on the main foil under any circumstances. If cavitation occurs and lift is lost on the wing, the ferry will drop and slam onto the water, resulting in an uncomfortable and potentially dangerous experience for passengers. According to SNAME (Society of Naval Architects and Marine Engineers), vessels must always have pitch attitudes confined between $\pm$ 5 degrees, and roll attitudes of $\pm$ 10 degrees (Miles et al., 2007). Exceeding these values can lead to motion sickness and discomfort, reducing the overall passenger experience.

Finally, the weight estimate used in this thesis is provided by the vessel designer and is divided into the following elements: Structure, Propulsion, Electrical Systems, Nav & Comms, Auxiliary Systems and Outfit. The weight of all components, and their position along each axis, are expressed. As a result of this data it is possible to compute the vessel's mass moment of inertia about the principal axes. A summary of the weight estimate can be found in Appendix A.

4 Predicting forces and moments

In order to evaluate the forces and moments acting on the boat by means of the foil, a macro based parametric Excel spreadsheet is created to compute the lift, drag and side forces induced by a chosen foil design, which is valid for any boat attitude. Using these forces, the moments are computed. The intent of this tool is to have a simple program that can give an easy and rapid quantitative response to the lifting problem for different types of foil arrangements or geometries, airfoil shapes, initial angles of attack, boat speeds, centre of mass positions, ecc. The complete set of input variables considered by the program is found in Appendix B.1, while a screenshot of the spreadsheet is found in Appendix B.2. Lastly the complete Excel file is found in the archive folder, accessible via the provided link in Appendix F.

The forces generated by the main and T rudder foil are resolved along the X, Y and Z axis. The moments of these forces are generated about the axis through a centre of roll, trim and yaw for the vessel, which will be called: centre of rotation. This point changes instantaneously and is positioned along the vessel's centre line, due to symmetry, with the same longitudinal distance as the centre of gravity. Since it's vertical position cannot be ensured, several positions are tested and the point is decided to be placed in the worst case scenario: as high as possible, but below the CG. The larger the distance between these two points, the larger the moment created by the centrifugal force (acting in the CG).

4.1 Definition of the frame of reference

To study the problem, a frame of reference is to be defined. A right handed frame is used, with the X axis pointing in the longitudinal direction, with positive values increasing towards the bow of the vessel. The Y axis is chosen to point in the transversal direction, with positive values increasing towards the starboard tack. As a consequence, the Z axis points in the vertical direction and the orientation is the same as the gravity vector, hence towards the bottom of the vessel. The origin of the axis is placed in the intersection point between the leading edge of the main foil, the centre line of the vessel and the underside of the main hull keel.

Given this frame, all angles and moments are taken as positive clockwise, hence positive rolling moments induce the vessel to roll to starboard, positive pitching moments induce the vessel to move bow upwards and positive yawing moments induce the bow to starboard. It is evident that negative moments induce motions in the opposite directions respectively.

4.2 Hydrodynamic forces

The spreadsheet is created based on the the Prandtl lifting line theory, chosen due to the geometry of the elements, which fits with the characteristics of this method. This theory is based on the assumption that, even though in reality the flow around an airfoil is non linear, it may be approximated by a linear summation of flows around the elemental aerofoils. In fact, only 2D rectangular shaped wings are considered (hence with no thickness) with the respective centre of pressure of each foil positioned at one fourth of the total wing chord. Also, no interactions between adjacent elements are considered. Once the elementary forces (lift and drag) for each element are computed, these are decomposed along the three principle axis and denoted with *lift* (the component along the Z axis), *drag* (the component along the X axis) and *side force* (the component along the Y axis).

The lift and drag forces are calculated on each foil using Equations 2 and 3:

$$L_{section} = \frac{1}{2}\rho A V_{app}^2 C_l^{3D} \tag{2}$$

$$D_{section} = \frac{1}{2}\rho A V_{app}^2 C_d^{3D} \tag{3}$$

where ρ is the water density, the area of the wing is denoted with A, while V_{app} is the apparent fluid velocity which the foil sees and C_l^{3D} and C_d^{3D} are respectively the three-dimensional coefficients of lift and drag. These hydrodynamic coefficients are the corrections of the two-dimensional coefficients, taking into account the different behaviour of the flow along the length of the wing, which is caused by the tendency of the fluid to slip from the high pressure surface to the low pressure one, creating a tip vortex. What influences such phenomenon is the ratio between span and chord of the wing (denoted as AR: geometric aspect ratio) and the 2D coefficient. In turn C_l^{2D} and C_d^{2D} are specific to each airfoil shape, the apparent angle

of attack and the apparent flow velocity. The formulas for the three dimension coefficients are presented between Equations 4 and 5:

$$C_l^{3D} = \frac{C_l^{2D}}{1 + 3/AR} \tag{4}$$

$$C_d^{3D} = C_d^{2D} + C_{di} \tag{5}$$

with

$$C_{di} = \frac{C_l^{3D}}{\pi \cdot AR} \tag{6}$$

At this stage C_l^{2D} and C_d^{2D}, together with the stalling characteristics of each section, were generated using data provided by Airfoiltools.com based upon X-Foil for both laminar and turbulent flows. To reduce errors, a linear interpolation between sampling points is done.

In the preceding formulas, the geometric aspect ratio AR is multiplied by a coefficient which enhances the influence of the ratio into Equations 4 and 6. This is used to tune the calculated results with the ones obtained with a more reliable, but also computationally expensive, RANS based CFD simulation.

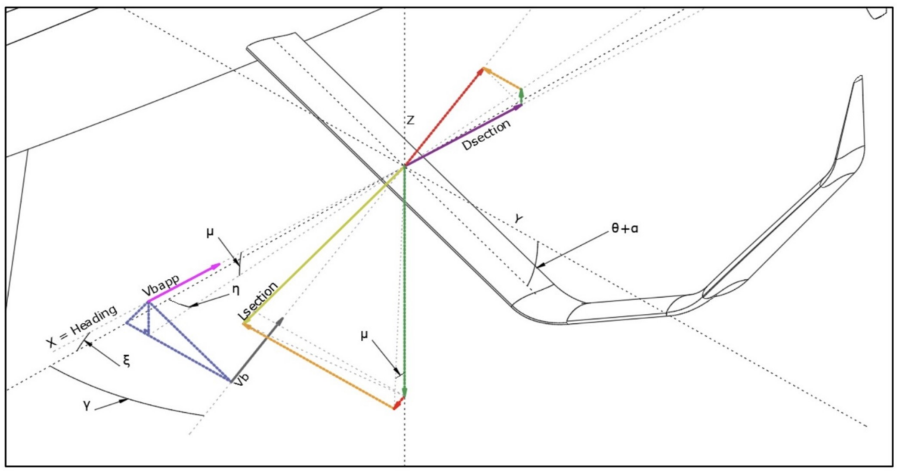

Figure 2: Force and velocity vectors show the AoA_{app} & V_{app}

Necessary to calculate the C_l^{2D} and C_d^{2D} are the apparent angle of attack and the apparent flow velocity. These can be obtained by resolving the velocity vectors, as shown in Figure 2.

The following equations are obtained to calculate V_{app} and AoA_{app}:

$$V_{app} = \sqrt{[V_b \cdot sin\gamma \cdot sin(\alpha + \theta)]^2 + [V_b \cdot cos\gamma]^2} \tag{7}$$

$$AoA_{app} = tan^{-1}\left(\frac{V_b \cdot sin\gamma \cdot \cos(\alpha + \theta)}{V_b \cdot cos\gamma}\right) \tag{8}$$

From Equation 8 it is obvious that a non null drift angle will increase the angle of attack seen by the foil, if the latter is not parallel to the free surface. Practically, given a positive drift angle, foil elements which happen to be pointing upwards will have an increasing apparent angle of attack, while for elements pointing downwards, the apparent angle of attack is decreased. Vice versa happens for negative drift angles.

Once computed the elementary forces parallel and perpendicular to the airfoil, these are decomposed along the three main axis by multiplying each vector along X, Y and Z directions. Unit vectors are developed into the Excel spreadsheet in order to project all vectors appropriately for any boat's or rudder's attitude or initial angle of attack. The way the unit vectors are constructed will be presented in Chapter 4.3 when the point of application of each force are computed.

During the calculation of the forces on the central foil, since the struts act as end plates, hence the aspect ratio is considered as infinite and the flow is expected to be constant along its span, 3D lift and drag coefficients are replaced with their 2D version.

The ride height of the hull above the water free surface (sink) and its roll angle are taken as variable parameters, hence the rolling and pitching motions of the ship influence the submerged area of the vertical foil sections (both of the main foil and the rudder), therefore having an effect on the generated force.

In the calculation of the rudder forces, the rudder's lift is calculated according to the relative angle between the rudder and the fluid flow, which is given by $\gamma + \beta$. The method does not consider the influence of the wake induced by the main foil on the rudder, for this reason the forces created by the rudder must be reduced by a loss factor, which is again tuned by means of RANS based CFD simulations.

4.3 Positions

As introduced earlier, the hydrodynamic forces are applied at the centre of pressure, which are approximated at the quarter chord of the wing. The position of the centre of pressure varies with flow speed and with angle of attack, but for the purpose of this analysis the position of this point will be considered to be independent of the just mentioned variables, and will always be at $1/4^{th}$ of the airfoil's chord. In order to obtain the position of such points in the global frame for any possible vessel's attitude, several different rigid transformations are applied. Firstly, the initial angle of attack is considered: a rigid transformation is made for every point considering the leading edge of each section as centre of rotation for every element. Later, a new rotation is done about the global centre of rotation to take into consideration the effect of roll, pitch or yaw attitude.

All rotations are achieved by firstly performing a rigid translation by computing the position of the point of interest in new coordinates, which have the origin placed in the local centre of

rotation. Secondly, a rigid rotation is performed by solving the following matrix equation:

$$R = R_z(\gamma) \cdot R_y(\zeta) \cdot R_x(\theta) \tag{9}$$

where $R_z(\gamma), R_y(\zeta)\ and\ R_x(\theta)$ are the rotations about the three main axes, which are respectively the Z axis, the Y axis and the X axis. The choice of performing the rotations in such order is to perform rotations from the smallest to the biggest angles. It is customary to have the largest attitude being the roll, then the pitch and finally the yaw. The rotation matrices are shown below:

$$R_z(\gamma) = \begin{bmatrix} cos(\gamma) & -sin(\gamma) & 0 \\ sin(\gamma) & cos(\gamma) & 0 \\ 0 & 0 & 1 \end{bmatrix};\ R_y(\zeta) = \begin{bmatrix} cos(\zeta) & 0 & -sin(\zeta) \\ 0 & 1 & 0 \\ sin(\zeta) & 0 & cos(\zeta) \end{bmatrix};\ R_x(\theta) = \begin{bmatrix} 1 & 0 & 0 \\ 0 & cos(\theta) & -sin(\theta) \\ 0 & sin(\theta) & cos(\theta) \end{bmatrix} \tag{10}$$

Of course this is the general formulation for rigid rotations, the angles of rotation are adapted according to every case; for instance, rotations induced by an initial angle of attack on the central foil have the following shape:

$$R = R_y(\mu) = \begin{bmatrix} cos(\mu) & 0 & -sin(\mu) \\ 0 & 1 & 0 \\ sin(\mu) & 0 & cos(\mu) \end{bmatrix} \tag{11}$$

with μ being the initial angle of attack.

The same procedure is also done on the rudder foils; however, in this case an additional rotation can be performed about the Z axis so to consider the rudder steering and about the Y axis so to consider for elevator deflections. It is to be noted that, the relative attitude of the rudder to the vessel must be considered when computing the angle of attack of the rudder with respect to the flow.

4.4 Additional forces

The other forces, which are included in this framework, are the gravity force, the centrifugal force and the thrust force induced by each propeller.

The gravity force is always acting downwards and is given by:

$$F_g = m \cdot g \tag{12}$$

The centrifugal force is an apparent force which appears when facing turns and is given by:

$$F_c = \frac{m \cdot v^2}{R} \tag{13}$$

with R being the trajectory radius.

According to the installed power on board, the thrust percentage (ϵ) and the velocity of the boat, the force induced on each of the two bulbs is calculated as follows.

$$F_t = \frac{P \cdot \epsilon \cdot 1000}{v} \tag{14}$$

4.5 Moments

Once the magnitude of all forces and their projections along the principle global axis are obtained, as well as their point of application, all moments are computed about the global centre of rotation of the vessel. X, Y and Z moments are calculated separately by checking if each force induces a clockwise or anticlockwise torque. Finally all the addends are summed up to obtain the total moment acting on the vessel about each axes.

4.6 Macros

Several macros are developed to further assess the response of the vessel in different conditions.

Stability must be assessed from an equilibrium condition, meaning that the sum of all forces and all moments acting on the vessel are null. This is achieved only once the main foil and rudder dimensions are fixed, by controlling the main foil angle of attack, the rudder angle of attack and the engine throttle. The inbuilt Excel solver is used to solve optimization problems given certain constraints and objectives. First of all, the appropriate angle of attack on the main foil is found by balancing the sum of the vertical forces (along the Z axis). Then the engine throttle is found by balancing the sum of the longitudinal forces (along the X axis) and finally the rudder elevator angle of attack is found by balancing the sum of the pitching moment (about the Y axis). All other force or moment components are intrinsically null due to the symmetry of the problem. This optimization loop must be solved several times before reaching the vessel's equilibrium condition, and for this reason a macro is developed.

Next, to perform a static stability analysis, an additional macro is developed which measures the forces and moments along or about each axes with the variation of only one variable at a time, namely the vessel's global pitch, roll and yaw angles, and also the rudder pitch and rudder yaw angles relative to the vessel. The resulting curves are obtained by assuming all, apart from one angle, set to zero, and the one angle under review is set incrementally (0.1 degrees) from -5 to +5 degrees. Results of this analysis are found in Chapter 7.

An additional macro is created which assesses, for a given set of roll, pitch, yaw and rudder positions, the minimum allowable turning radius for which the vessel banks into the corner. For turning radii larger than the minimum allowable radius, the boat banks into the turn and vice versa. The limit of this analysis is that the knowledge of the vessel's attitude in all directions is needed and this is not possible uniquely with a static analysis such as the excel spreadsheet. A more detailed dynamic simulator should be used to assess the allowable turning radius.

4.7 Comparison with CFD

The use of the lifting line theory inevitably brings some discrepancies with more accurate RANS based calculations. In terms of time, initial CFD simulations are made at this stage, and the results are used in the following sections. The methods used to obtained the results will be presented in Chapter 10.

When comparing the obtained results, different correction coefficients should be used for different speeds, angles of attack, ecc. Instead of scalars, a more precise transfer function could be developed to better compensate the differences the two methods bring, but it is believed that the spreadsheet doesn't aim to be as precise as a CFD simulation, instead it desires to be a fast and effective tool to assess different foil geometries. Due to the fact that the CFD simulation is based on a single phase fluid, where the free surface interface is not modelled, the strut simulation is believed to be far from reality, for this reason the correction factor is only used on the fully submerged foil sections.

For what is said, a scalar is identified for each foil section to better match the two algorithms. The scalar is identified by calculating the average between the correction factor for winglet angles ranging between ± 15 with a step of 5 degrees, as well as different flow velocities corresponding to the lift-off, cruise and maximum speed. Instead, for the rudder, as well as the different speeds, 5 different angles of attack are tested. It must be noted that the downwash effect of the main foil on the elevator is not accounted for in this framework.

The summary of the scalars, for each section, are 1.4 on the two winglets, 0.7 on the central foil and 0.8 on the elevator foil.

5 Geometry definition

To ensure maximum efficiency, the beam of the main foil must be as wide as possible. By doing so, the geometrical aspect ratio, hence as stated in Equation 6 the induced drag, is reduced. To allow the vessel to be docked laterally along the port or starboard side and reduce any interference with the dock, the total width of the main foil is controlled by the total beam of the boat. Knowing these dimensions, the mean aerodynamic chord is computed to counterbalance approximately 85% to 90% of the total weight of the vessel.

The vertical mast dimensions are limited by the strength that the pylons are able to produce, more in particular, the chord and thickness are linked one another by the choice of the airfoil shape, while the chord is verified by structural means, which will be addressed in Chapter 11. The length of the struts are chosen so that the vessel can lift above the wave height, hence not being affected by the sea state. Data gathered from the Chichester Harbour buoy (located at the east end of the Solent) is used to understand in more detail the sea state which the

vessel will need to face. The average significant wave height measured in the last 12 months is equal to 1.1 m (National Costal Monitoring, 2023). Given the Froude similitude between the model and full scale vessel, a model scale wave height equal to 0.495 m is calculated (for simplicity this figure is approximated with 0.5 m). By ensuring that the foil is at least 0.25 meters submerged into the water, and that the required clearance between the wave crest and the bottom of the vessel's keel is 0.25 m, the minimum vertical strut component must be equal to 1 m.

At both extremities of the central foil, beyond the vertical struts, the horizontal foil can extend itself, followed by one angled winglet at each end of the main foil, to aid stability. The angle the winglet has with respect to the horizontal plane, it's chord and span, as well as the span of the port or starboard side horizontal foil, are all input parameters to be chosen according to lateral stability: the bigger the winglets, the larger stability is achieved.

It is customary that the main foil creates between 85% and 90% of the total lift generated, while the rudder elevator creates the remaining portion of lift. According to this statement, the lift generated by both wings must have the same sign, and the allocated fraction the rudder must create is hence computed. In order to have a longitudinal statically stable configuration (stability will be assessed in more detail in Chapter 7), the centre of gravity is chosen to be positioned between the main-foil and rudder wings. More in particular, the longitudinal centre of gravity position must be fore of the aerodynamic centre of the whole foil system to ensure adequate static stability. On the other hand, if the centre of gravity is positioned too fore, the required control forces become very small, meaning that the vessel's attitude is very sensitive to the rudder orientation. The rudder's vertical strut is sized so that the rudder can create a larger moment about the vertical axis than the opposite one of the main foils. In this way it is possible to change the heading (yaw attitude) of the vessel.

By running the first macro presented in Chapter 4.6, it is possible to find, if it exists, the main foil and rudder angles of attack, as well as the engine efficiency, necessary to reach an equilibrium condition.

Based on these considerations, a preliminary sizing of each foil section is created.

6 Power prediction

Based on the forces predicted in Chapter 4 and towing tank tests conducted by Professor Giles Barkley on the displacing vessel, the resistance plot is presented in Figure 3. The hull shape was chosen as a trimaran as Prof. Barkley proved that this configuration produces the least drag. The analysis produced is based on a 1.5 meter model, manufactured using the Solent University facilities and tested using the University's towing tank. The results are scaled to the 9 meter vessel using a scaling method, which takes into account the trimaran

reducing displacements as the boat lifts out of the water, and the correct drag on the foil including Reynolds number effects.

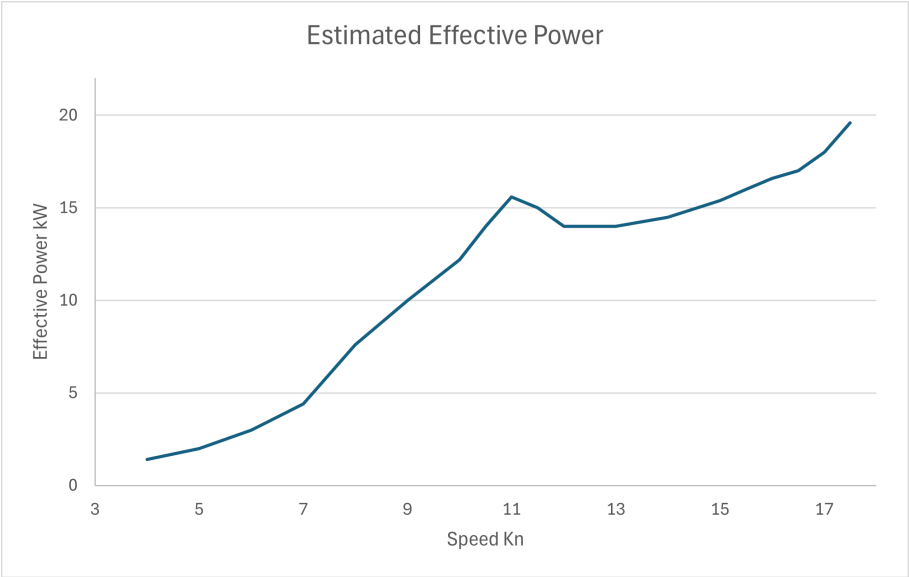

Figure 3: Estimated effective power

The power required by the vessel increases linearly until the vessel begins to lift off from the water surface. At this stage, since the hull is no longer in the water, the resistance drops, reaching a new local minimum. After this point, the resistance continues to rise exponentially. The design goal is to position the vessel's cruising speed close to this local minimum, reached between 12 and 13 knots, with a maximum speed requiring power close to that needed for lift-off. This ensures that the installed power is optimized for both conditions, while minimizing power consumption during the large part of the vessel's navigation.

Once the final foil geometry is ultimate, the tank test should be performed once again and compared with the power produced by the propellers to ensure that the these can push the vessel into foiling mode and sustain the vessel at the aforementioned speeds.

7 Static stability analysis

Stability is assessed to ensure that during flight, the vessel can return to an equilibrium condition. In order to ensure the maximum level of safety, a statically stable configuration is searched, meaning that if the vessel is disturbed from equilibrium, the hydrofoils must create a restoring moment opposite to the angle of attack of the disturbance. For example, if the

vessel were to encounter a gust of wind, which would pitch the bow up by 2 degrees from its intended straight line course, then a negative moment is desired, which would push the bow down to the previous equilibrium condition. Vice versa, if the disturbance were to be negative, the restoring moment would need to be positive to push the bow upwards. This example can be extended about any axis.

Stability must be assessed starting from an equilibrium condition.

7.1 Stability curves

Static stability is assessed uniquely at the speed of 13 knots to consider the dynamic forces generated by each section of the foil, as this is the most frequent speed condition. Three static stability graphs show how the moments about each axis change with the variation of only one variable at a time, namely the vessel's global pitch, roll and yaw angles, and also the elevator pitch and rudder yaw angles (which are relative to the vessel). The resulting curves are obtained by varying, one at a time, the variables between ± 5 degrees, with the one angle under review set incrementally at 0.1 degree intervals.

The tested geometry is based on the considerations presented in Chapter 5, together with best engineering judgement.

7.1.1 Directional stability

Directional stability pertains to the control and stability of the yaw motion, which is necessary to maintain the intended course and respond predictably to steering inputs. The yaw moment analysis, presented in Figure 4, indicates that the pitch and elevator angles, as well as the roll angle, have minimal influence on the yaw attitude of the vessel; instead, the primary contributors to yaw moments are, as expected, the change in drift and rudder angles as these sections create the majority of their force in the vessel's transverse direction. The self-righting nature of this moment, as indicated by the crossing of the second and fourth quadrants of the cartesian axis of the curves, is a desirable characteristic for maintaining directional stability. This self-righting behavior ensures that the vessel naturally returns to its equilibrium yaw position after a disturbance. The main parameters which influence the directional stability are the strut size, the rudder blade size and the ride height.

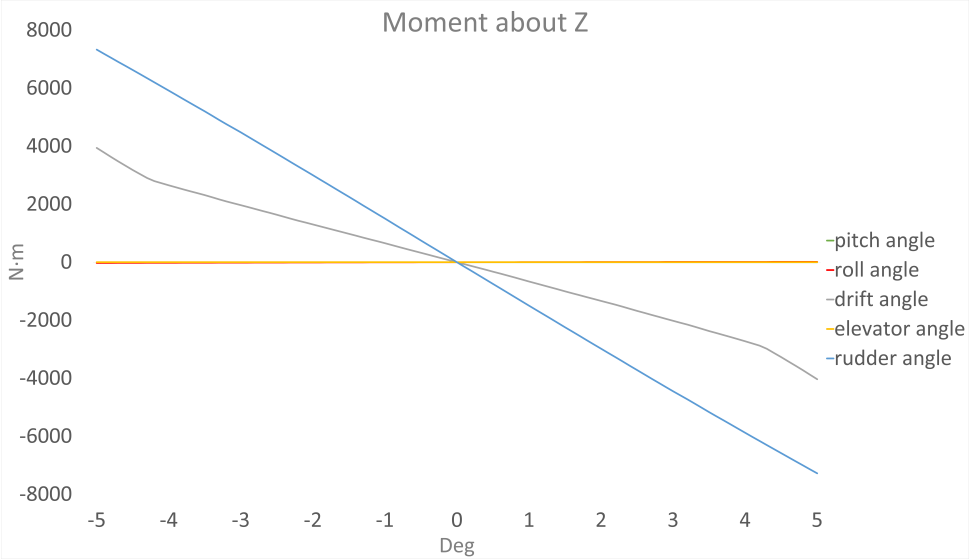

Figure 4: Directional static stability

When the rudder is moved during navigation, a roll and a yaw moment are created. The latter induces the vessel to turn (which is a positive & wanted feature), and by doing so, an opposite drift angle is seen by the main foil struts which, in turn, produces a side force which happens to turn the vessel even more. With this being said, if the rudder is free to rotate (not generating any force), the vessel will tend to reach a heading opposite to the water flow. Instead, if the rudder angle is smaller than the drift angle, then the rudder creates an opposing moment which gives control to the yaw rate and allows a smooth change in yaw angle. This means that the rudder is not used to induce a turn, but it is needed to correct the heading of the vessel and to control the rate of turn. Once the desired heading is reached, the rudder is returned to a neutral position (or in an extreme case to the opposite side of the turn) to induce a total restoring moment which can return the vessel to a straight course. Moreover, the yaw moment generated by the rudder (shown in blue in Figure 4) is significantly larger than that produced by the main struts. This indicates that the rudder plays a critical role in controlling the yaw attitude, providing the necessary corrective forces to maintain directional stability.

From what has been said, the rudder must be sufficiently large to recover the vessel from a disturbance, hence to create an opposing yaw moment larger than the one created by the struts. The maximum yaw angle that the vessel may face during flight is equal to 5 degrees, hence this will be used as reference angle which the rudder must be able to recover from. This same data will be also used in Chapter 9 to assess the rudder airfoil shape selection.

7.1.2 Longitudinal stability

Longitudinal stability concerns the control and stability of the pitch motion. This stability is vital for maintaining the vessel's trim and ensuring smooth operation in varying sea conditions. The pitching moment analysis, depicted in Figure 5, shows that changes in the roll angles have negligible influence on the pitch attitude of the vessel. In contrast, both positive and negative drift angles, as well as rudder angles, consistently create a slight negative pitching moment. This tendency for the bow to pitch downward is due to the additional drag created below the center of rotation when the struts are at a yaw angle (both to port and starboard).

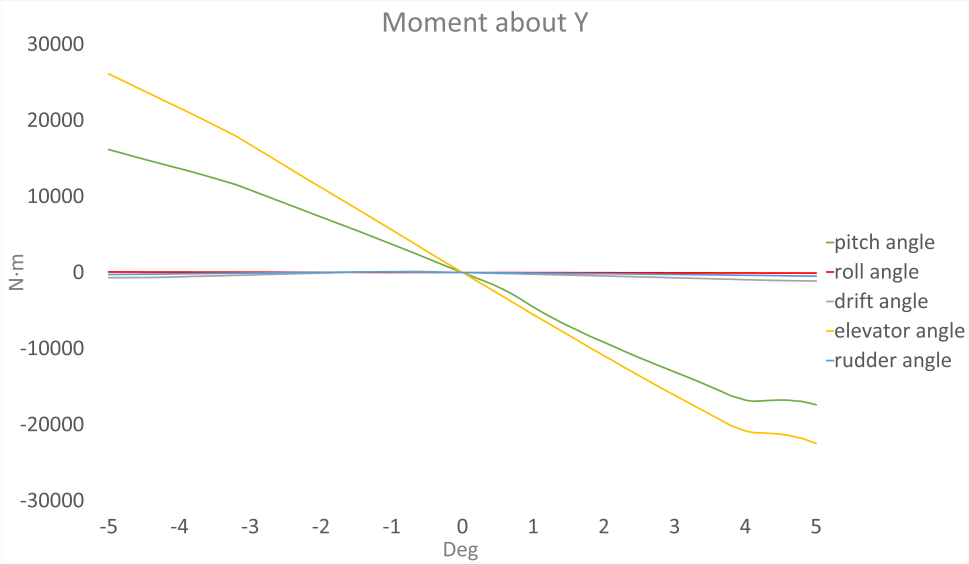

Figure 5: Longitudinal static stability

The most significant factors affecting the pitching moment are the vessel's global pitch angle and the rudder pitch angle. In both cases, the resulting moment is a restoring moment, which is critical for maintaining longitudinal stability. Notably, the pitching moment generated by the elevator is consistently larger than that produced by the main foil. This implies that the elevator has a substantial capacity to control the vessel's attitude, providing the necessary corrective forces to maintain longitudinal stability.

If there is a desire to change the trimaran's ride height, the elevator is trimmed, creating a pitching moment which changes the attitude of the vessel. To return to an equilibrium position (pitch angular velocity equal to zero), the elevator can be straightened and a restoring pitching moment brings the vessel back to equilibrium. For this reason, note that the elevator must be sufficiently large to overcome the main foil moment, allowing the vessel to change pitch attitude. A larger elevator can improve response times for pitch corrections, but may also lead to overcorrections, potentially destabilizing the vessel.

Although the longitudinal stability could be further improved by reducing the coupling effects with the drift angle, this configuration is anyways promising because the main foil helps the vessel maintain the desired trim, and the elevator being able to correct the global longitudinal attitude of the vessel. Unfortunately, it is impossible to reduce this coupling phenomenon since an increase in drift angle inevitably creates drag below the CG (an increase in force is in the X direction with the same lever in the Z direction increases the moment about Y), this effect is mitigated by including the thrust input as part of the PID control loop system, which can actively change the thrust to maintain the desired pitch attitude of the vessel.

7.1.3 Lateral stability

Lateral stability concerns the supervision and stability of the roll motion, which is crucial for maintaining the vessel's equilibrium. The lateral stability of a hydrofoiling vessel is primarily influenced by the roll, drift, and rudder angles.

When analyzing the roll moment, it is observed that the vessel exhibits a slight stability for positive winglet dihedral angles (winglets pointing upwards), which becomes instability for anhedral winglets. The degree of stability (or instability) depends on the distance of the winglets from the global centre of rotation: short struts improve stability while longer struts worsen lateral performance, at the point that tips pointing downwards produce a self righting vessel instead of ones pointing upwards. This happens because the moment created about X is created between the competition of forces along Y with a lever arm in Z, and forces along Z with a lever arm in Y. As the strut length increases the influence of the force along Y is greater, hence tips pointing downwards must be preferred; instead if the strut length is short then the vertical force component is relevant and tips pointing upwards perform better. In this particular scenario, for vertical struts which are 1 meter tall, winglets pointing upwards are chosen.

Note that, to turn the rudder is set at an angle and the vessel drifts in the opposite direction of the turn (pointing in the centre of the turning circle), meaning that the rolling moment created by the rudder and the struts are opposite, counterbalancing each other. Looking at Figure 6 quantitatively inside the studied domain, the rudder would theoretically be able to correct a roll moment created by the struts, if the maximum drift angle was 1 degree, by turning the rudder to 1.5 degrees (the latter is the relative angle to the flow, hence the absolute value of the rudder angle must be closer to 2.5 degrees). Therefore, it is essential to ensure that when turning, as a guide, the drift angle must be no larger than 66% of the applied rudder angle. A further analysis, based on the balance between the equivalent lift force generated by the two main foil struts and the centrifugal force, which pushes the vessel out of the trajectory radius when turning, shows that the drift angle should be no more than 0.974 degrees for a turning radius equal to 75 meters. This analysis was conducted at the speed of 13 knots with a generic airfoil shape which produces a lift coefficient equal to 0.01 times the angle of attack seen by the struts.

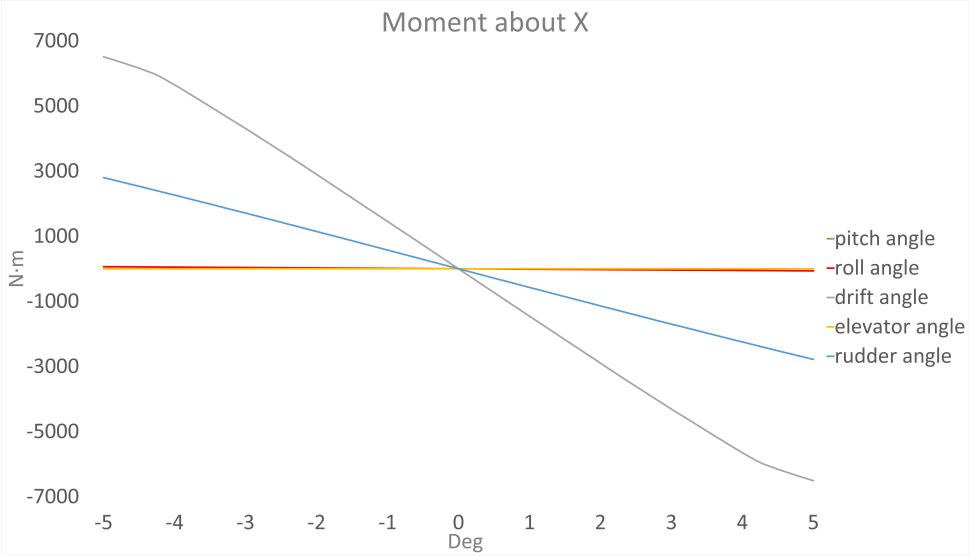

Figure 6: Lateral static stability

The results of this analysis, which are the upper limit of the drift angle, show that indeed the drift angle is confined between acceptable values which the rudder is able to recover from. More in particular, the moment created by the drift, are smaller than the ones necessary to counterbalance the rolling imbalance produced by the rudder when turning, suggesting that the vessel may bank inside the turn excessively before actually performing a turn. In the same framework it is proven how, by banking inside the desired turn, the turning abilities of the vessel are increased (Meyer, 1994). This was further confirmed by the forces and moments Excel spreadsheet.

This is the most worrying stability assessment due to the strong influence of the rudder blade on the vessel's roll moment, this effect must be mitigated by the vertical struts or by using a different technique. As the rudder is adjusted to reach the desired heading, the vessel drifts; the lift produced by the flow on the two sections (rudder blade and main foil struts) is opposing and a balance must be reached. The limitation is that there is, due to the different vessel's inertia about each axis, a delay between the roll moment induced by the rudder and the change in drift, which in turn corrects the unwanted roll moment. Additionally, the just presented equilibrium is very dependant on the vessel speed and sea conditions, hence a sophisticated flight control system must be used to support the vessel during turns. To sum it up, the vessel's rolling abilities can only be fully assessed by means of a dynamic analysis.

7.2 Improving the rolling abilities

Without the implementation of a flight control system algorithm, which goes outside the scope of this work, different potential methods to improve the rolling abilities of the hydrofoiling ferry are presented:

7.2.1 Winglet ventilation

This proposal consists of ventilating the hydrofoil with high pressurized air, which is forced to mix up the laminar flow around the airfoil and reduce the lifting abilities of the considered section of the hydrofoil. This can be achieved by creating some small cavities on the surface of the wing winglets which are connected to some hoses inside the core of the wing. The air tubes, which run from the winglet, along the wing span and up the strut, are connected to a high pressure air tank located inside the hull via two electrovalves, the first one normally-closed, which acts as the primary valve, and the second one normally-open, which acts as a redundant valve and gets into action only if the first fails.

A ventilated wing reduces the lifting abilities of the wing, but inevitably creates additional drag. This is modelled in the spreadsheet with the lift force being multiplied by the factor (winglet efficiency)/100 and the drag force multiplied by the factor 100/(winglet efficiency). After testing different scenarios, it is shown that this idea has the potential of improving the rolling capabilities and control of the vessel for any attitude, more in particular it is shown how, when performing a left side turn, the reduction in lift of the starboard winglet is able to create a smaller anticlockwise moment about X which enhances the vessel to bank into the turn. The reduction of such forces can improve the rolling abilities of the vessel.

The inevitable consequence of this concept is that a large force in the longitudinal direction is created, which increases drag and generates moments about the Y and Z axis. The MY moment pushes the bow down, which as seen earlier, can be mitigated with an active control system on the electric motors. On the other hand, MZ is a righting moment which returns the bow into a straight course, hence not being a concern. According uniquely to the Excel model, this technique, using the multiplying factors presented above, is able to correct a 3000 N·m rolling moment. This concept can work for any ride height and in any condition, additionally, before lifting off, no further drag is created. The valves can be included in the flight control PID loop to actively improve the rolling behaviour of the trimaran during flight. The need for additional housing for the air tubes through the vertical struts is not necessary as the housing is already created to host the electrical cables, necessary for the motors to be powered.

This concept must be validated via tank tests.

A similar concept can be used on the whole wing (or only the central portion of the wing), to control the minimum sink of the vessel. Small communicating cavities are made from the wing surface, up into the strut. When the hole on the strut is submerged, then the difference in water pressure between the two extremities of the cavity will create water to flow, without any negative effects. As soon as the hole on the strut is out of the water, the difference in pressure between the immersed and emerged hole will create a flow of air from the hole in the strut down to the wing causing ventilation, thus making the wing drop down again until the hole in the strut is submerged again.

Note the effects of ventilating close to the propeller may need some consideration.

7.2.2 Additional foil stabilizers

This idea consists in placing two additional hydrofoil winglets, which will be called stabilizers, positioned outwards from each strut and just above the free surface when foiling. As the vessel heels, the inner stabilizer can drop into the water and create a counteracting moment able to push the vessel back to level. The stabilisers must not extend past the breadth of the vessel, as stated for the winglets in Chapter 3; in the same vein the stabilizer root chord is the same of the struts to maintain continuity.

If the stabilizers are to be effective for small roll angles, then their root must be placed exactly on the free surface, instead, if they are desired to be effective at larger angles, the root of the stabilizers can be placed further away from the free surface. This distance can be changed during flight by varying the sink value to adapt the need for different conditions. The angle of the stabilizer wings with respect to the horizontal plane is decided according to how quickly the righting moment must be applied for increasing roll angles: stabilizers pointing downwards will drop quickly into the water at small roll angles resulting in a steep stability curve, while stabilizers pointing upwards will drop more slowly into the water resulting in a more gradual slope; in this way the best window where the stabilizers can work is created. By increasing the initial AoA of the stabilisers, or by changing airfoil section or its planform area, the maximum righting moment can be increased. The benefit of such system is that the stabilizers may be swapped easily according to the sea state or other conditions to best adapt the arrangement (for example stabilizer angle, airfoil shape or length) to the vessel's needs.

This concept can work as planned only for a particular ride height, highlighting its limitations when the helm requires the vessel to fly at a different ride height. Additionally, when the vessel is in displacement mode before lifting off, the two additional foils create unwanted drag at low speed but additional lift at higher speed, which respectively hinders or helps the vessel to foil. These stabilising foils inevitably have effects on the longitudinal stability: when the vessel is heeled, the stabilizers are submerged creating additional drag below the centre of rotation which creates a pitching down moment. For example a low drag section profile can improve such shortcomings, or as stated earlier, the separate use of the port and starboard propellers can be implemented inside the control system algorithm to improve longitudinal stability.

8 Testing different geometries

Since the stability curves are mostly linear, values are obtained for roll, pitch and yaw angles, as well as rudder and elevator angles equal to 2 degrees.

Data for the rudder and the main foil angle of attack, as well as the throttle power, that are required for the vessel to be in equilibrium are also considered. The throttle is a representation

of the drag produced by a given configuration: higher values mean that the system produces more drag, hence more throttle is needed. The maximum possible throttle is equal to 100%, where the whole 40 kW installed will be needed to maintain the vessel in equilibrium without considering any type of loss. On the other hand, smaller values of throttle mean that less power is required to maintain the trimaran in equilibrium. Obviously small throttle values are preferred.

8.0.1 Objectives for the optimization of the design

To perform an optimization of the stability of the vessel, objective values for each quantity are be identified.

Change in roll

- **Moment about X:** This result shows how a change in roll angle affects the X moment, meaning that if the vessel is heeled by 2 degrees to starboard, a 25 N·m torque is created which induces the vessel to heel even further. This value must be as negative as possible for it to be the best restoring moment.
- **Moment about Y:** This result shows how a change in roll angle affects the Y moment about, meaning that if the vessel is heeled by 2 degrees, a negative restoring - 41 N·m torque is created which induces the vessel to pitch bow down. To reduce the coupling effect between different axes this value must be as close to zero as possible.
- **Moment about Z:** This result shows how a change in roll angle affects the Z moment, meaning that if the vessel is heeled by 2 degrees, a 3 N·m torque is created which induces the vessel to drift with the bow to starboard. To reduce the coupling effect between different axes, also this value must be as close to zero as possible.

With the same idea all other components are analysed: coupling effects should be reduced and restoring effects should be enhanced. When analysing the rudder and elevator, the restoring effects these have, must be larger than the ones given by the main foil to improve the controllability of the vessel in both pitch and yaw. For this reason, the change in elevator-Y moment and change in rudder-Z moment curves should respectively be steeper than the change in pitch-Y moment and change in yaw-Z moment curves.

If the restoring moment is too large, the vessel might oscillate around the equilibrium position without reaching stability. For example, if a gust of wind causes a 1 degree disturbance, a -1000 N·m moment would act to restore the vessel. As the vessel's angle decreases to 0.5 degrees, the restoring moment halves. The torque continues to act until the vessel reaches 0 degrees, where the torque is null. However, the vessel's inertia may cause it to overshoot, creating an oscillating pattern with alternating positive and negative disturbances. What mitigates this effect is the damping of the system which reduces the oscillations over time. Since water is much denser and more viscous than air, high damping is observed (Bai et al., 2010). The damping ratio ζ, is a dimensionless measure describing how oscillations decay

over time and is equal to $\zeta = \frac{C}{2 \cdot \sqrt{I \cdot K}}$ with C being the damping coefficient, I is the moment of inertia of the vessel about the respective axis and K is the stiffness coefficient, which corresponds to the slope of the restoring moment curve. The high damping coefficient typical for hydrofoil generally creates an overdamped system (or in some cases a critically damped one), leading to minimal oscillating concerns (Münch et al., 2010).

8.0.2 Analysis of different designs

Given the objectives, many different foil configurations are tested. A small part of results are found in Appendix C, while the complete set is found in the archive folder, accessible via the provided link in Appendix F. The top half set of results found are the absolute values of the static stability analysis for each configuration, while the second set are the relative percentage error of each configuration with respect to the reference one. This means that if the percentage is positive, there is an improvement of the stability, while if the percentage is negative, this suggests that there is a decrease in stability.

The centre of rotation changes dynamically during navigation according to the vessel's trajectory and motion, for this reason this point is positioned in the worst case scenario. Several CR positions are tested and the outcome of the analysis is that the higher the CR (always below the CG), the worse stability the vessel has. To be on the safe side, the centre of rotation is positioned 100 mm below the centre of gravity.

1. Winglet angle with respect to the horizontal plane

   Following what was introduced in Chapter 7.1.3, small angles are preferred for efficiency, but at the same time winglets pointing upwards produce a self righting vessel in roll, while winglets pointing downwards create instability. The greater the winglet angle, the stronger the effect on stability, so highly upwards pointing winglets should be preferred. However, upward winglets increase coupling effects between yaw motion and roll or pitch moments. To minimize these coupling effects, downward pointing winglets are preferable.

   Since, a balance between these effects should be achieved, a positive winglet angle of 15 degrees is chosen.

2. Total main foil span

   By increasing the aspect ratio of the wing, the efficiency is increased significantly. All other variations are minimal, hence the widest possible main foil must be preferred for any chosen chord.

3. Strut angle with respect to the vertical plane

   The effect of the strut angle variation can be noticed with the yaw motions of the vessel: positive strut angles (veeing outwards, upwards) reduce coupling effects between the yaw

motion and the roll and pitch moments. The greater the strut angle, the greater the improvement.

From a structural design perspective, in addition to being subjected to compression, inclined struts are also subjected to bending, so this configuration is structurally more demanding compared to vertical struts. It must be noted that a V shaped strut pushes the connection to the hull further away from the centre line, potentially creating transversal twisting structural problems on the hull of the vessel. If this connection location is confined by hull design features, then the portion of wing enclosed by the struts (which act as end plates) is reduced, hence the foil's efficiency is reduced.

For what has been said, the strut angle must be as large as possible, remaining compliant with the structural requirements of both the hydrofoil and vessel. Hence, a positive angle of 10 degrees is chosen.

4. Winglet to main foil planform ratio

   The effect of varying the winglet area is negligible on the total efficiency (approx 1%). Larger winglet areas improve the rolling stability of the vessel but worsen the coupling between the roll motion and the pitch and yaw moments. Since the coupling moments were initially small, the effect of varying the winglet area is also small.

   For these reasons, a winglet to main foil planform ratio of 0.5 is chosen. This can be achieved by not having any horizontal section of the main foil beyond the struts, or by reducing the section of the main foil between the struts at the expense of reducing efficiency of the whole foil. Alternatively, the winglet chord could simply be increased. Given the three alternatives, the first one is preferred.

5. Elevator to main foil planform ratio

   A smaller ratio improves the overall efficiency of the vessel at the expense of reducing its pitch control abilities.

   The driving factor for the elevator design is the longitudinal stability, which was covered in Chapter 7.1.2.

6. Submerged rudder blade to single strut planform ratio

   Smaller ratios improve efficiency, as well as coupling effects between the roll and pitch moments together with the yaw and rudder angles; but as for the elevator selection, directional stability is the driving element which must be used for the rudder sizing.

7. Rudder & elevator longitudinal position

   A rudder which is closer to the main foil is more fuel efficient thanks to its smaller required AoA, but this reduces the vessel's righting abilities in both pitch and yaw motions. The longitudinal position is particularly relevant in the lift distribution between the main foil and the elevator, hence this is the key parameter which is tuned

to deliver 85% of the lift on the main foil, and the remaining part on the elevator foil. For this reason, the rudder's longitudinal position is set at 5.06 m from the main foil leading edge.

8. Centre of gravity and rotation longitudinal positions

   The variation of this parameter goes hand in hand with the rudder longitudinal position. A CG (hence also the X component of centre of rotation, since these points are modelled to be longitudinally coincident), which is positioned more aft is more fuel efficient, but simultaneously the righting abilities of the vessel in both pitch and yaw motions are also reduced.

   The CG is imposed by the weight estimate and only minor changes can be made. Several CG positions could be tested during sea trials by moving ballast weights on board between runs to better assess the influence of this parameter.

9. Ride height

   The ride height mostly affects the yaw behaviour of the vessel. In fact, in a lower flight condition, when the vessel is closer to the free surface, the MZ moment that the vessel produces in yaw or with a change of rudder, both improve, while the coupling between the yaw motion and the roll and pitch moments worsen.

   For this reason, several configurations should be tested during sea trials to assess the effective influence of this parameter on the abilities of the vessel and hence guarantee adequate stability.

10. Main foil to strut planform ratio

    The ratio between the vertical and horizontal foil sections greatly affects the moments given by the change in roll and change in yaw, as well as the efficiency. Larger ratios worsen the coupling between the rolling motion and the yawing moment, but at the same time all the other coupling effects are improved, as well as the self-righting and self-levelling abilities in roll and pitch. Additionally, slimmer struts have lesser of an impact in case of transverse seas, this aspect is beneficial due to the lack of flaps which help the vessel stabilize.

    Seen that smaller ratios have the additional benefit of improving efficiency, the smallest possible main foil to strut ratio is chosen, compliant with the structural strut requirements.

11. Main foil planform area

    After choosing the most appropriate ratio for all the parameters listed above, several main foil planform areas are tested. This variation changes the main foil aspect ratio as the span remains constant, which in turn will affect the angles of attack of the tested foil, and hence the efficiency of the vessel. The variation of this parameter influences also the MY and MZ moments created by both the global vessel angles and the rudder angles.

As the main foil planform area gets smaller, the moments become less significant, which also reduces coupling effects that benefit the design. Therefore, it's important to find a balance between these factors to reach the best compromise.

A main foil planform area between values of 0.635 m^2 and 0.685 m^2 is believed to be the most appropriate choice due to the improvement in efficiency and the reduction of the coupling effects.

8.0.3 Further considerations

- Improvement on roll stability during turns can be achieved by moving the centre of pressure of the main foil closer to the outer winglet, by doing this, a larger force is created on the outer section of the vessel to increase righting moment and reduce the change of capsizing. This can be achieved by adding twist on the outer portion of the winglets or by changing the airfoil shape for increasing span distance.
- Improvements on coupling between unwanted motions and moments can be reached if the vertical struts have a thinner connection to the main foil and wider connection to the hull. This solution could present some structural limitations.
- Rolling characteristics are improved with a low aspect ratio elevator.
- Sweep is not needed because the struts already offer the necessary directional stability the vessel needs.
- A shorter immersed vertical rudder blade will improve dramatically the unwanted rolling coupling between the change in rudder motion and the rolling moment. This goes in contrast with the idea of having the rudder in the water even if the main foil were to leap out of the water. The chance of having such a situation and the amount of time that the vessel can be fully uncontrollable is close to null, and for this reason improving rolling abilities is considered the better choice.

8.0.4 Optimized design

For all that has been said, the proposed 'optimised' configuration is described by the following dimensions:

MAIN FOIL DATA					
STRUTS	Total Main strut height	1,00	**m**		
	STBD Main Strut Underwater Span	0,50	**m**		
	Port Main Strut Underwater Span	0,50	**m**		
	Chord of Strut (Main Masts)	0,34	**m**		
	Angle of strb. Strut to the vertical plane	10	**deg**	0,175	**rad**
MAIN FOIL	Distance between struts (on main foil)	1,68	**m**		
	Span of Horizontal Main Foil	1,68	**m**		
	Chord of Horizontal Foil	0,38	**m**		
	Initial main foil angle of attack	4,33	**deg**	0,076	**rad**
	Bulb length	1,00	**m**		
WINGLETS	Span of winglets	0,97	**m**		
	Chord of winglets	0,33	**m**		
	Angle of stbd w. to the horizontal plane	15,00	**deg**	0,262	**rad**
	Initial winglet angle of attack	4,33	**deg**	0,076	**rad**
	Strb. winglet efficiency	100	%		

RUDDER FOIL DATA				
Total Rudder strut height	1,00	**m**		
Rudder underwater span	0,60	**m**		
Rudder chord	0,25	**m**		
Elevator span	0,80	**m**		
Elevator chord	0,20	**m**		
Initial rudder angle of attack	2,56	**deg**	0,045	**rad**
X distance of rudder origin	5,06	**m**		

Table 3: Optimized foil dimensions

The efficiency improvement, with respect to the initial foil configuration introduced in Chapter 5, is evident, as well as the self-righting rolling ability of the vessel. All the unwanted coupling moments are improved, except for the yaw moment created due to a change in roll. It must be noted how this component of moment created for such scenario is very small, hence although an improvement is not reached this is not considered to be relevant. Also smaller values of MY_{pitch} ,$MY_{elevator}$, MZ_{yaw} and MZ_{rudder}, are noticed compared to the ones given by the given geometry. Such large moments were considered as unnecessary, efficiency can be exploited whilst still guaranteeing the possibility to recover from a yaw disturbance of 5 degrees with a rudder angle of -2.8 degrees. All values larger than the latter value (from -2.7 to +12 degrees - stalling angle-) are rudder angles which are able to recover the vessel from excessive yaw angles. Instead, the elevator is sized according to the lift distribution between the two foils, in fact the proposed configuration distributes 83% of the total produced lift by the front main foil, and the remaining 17% from the elevator foil. This elevator is able to induce any pitch angle (up to 9 degrees -approximate stall angle-) and recover from it.

9 Airfoil selection

It is essential for the foils to be working in the most appropriate conditions in order to maximise performance. In this chapter the airfoils are selected for each element of the foil system.

For this scope http://www.airfoiltools.com/ is used as a database of airfoil shapes to choose from, while instead XFLR5 is used to modify the shapes and analyse them. The latter is a software based upon a Laplace Equation solver algorithm providing detailed information on pressure distribution, as well as the lift, drag, and moment coefficients across different angles of attack at different Reynolds numbers. It must be noted that all these analysis are preformed with a Reynolds number of 2.5 million, which approximately fits all the conditions for each element of the hydrofoil system.

The complete set of studied airfoils are found in Appendix D.

9.1 Main foil

Given the optimal geometric dimensions presented in Table 3, the C_L coefficient required by the main foil to maintain stable equilibrium flight in the different conditions are presented below:

	Kn	$C_{L\ 2D}$
Take-off speed	11	0,987
Cruise Speed	13	0,698
Maximum speed	15	0,521

Table 4: Required main foil C_L at different speeds

The foil requirements drives the research into airfoils capable of performing across all considered lift coefficients, without the use of any lifting surface. The condition with most importance is the cruise speed; however, also lift-off speed is crucial to overcome the resistance on the wetted hulls prior to flight. In this regard, the lift and drag coefficients are analysed with respect to one another or in relation to the angle of attack.

The moment coefficient instead is a direct consequence of the lift aerodynamic centre: the further forward the latter is of the quarter chord point, the more negative the moment coefficient is; instead the further back the aerodynamic centre is, the more positive the C_M is. In this design, the aerodynamic centre can be placed anywhere, as long as it doesn't move excessively during operations, resulting in large moment fluctuations which can disrupt stability. With this being said, there are two reasons for why the moment coefficient is not used as a key design characteristic for the main foil airfoil selection: firstly, the vessel will

operate primarily at cruise speed, the change of speed from displacement mode to foiling mode is just a brief transient condition that the vessel must surpass to enter the foiling condition. The time at which the vessel travels at 11 knots and the effect of a changing C_M are believed to be minimal. Secondly, a trim control system will guarantee level flight, meaning that the trim attitude of the ship is driven by the PID loop and not by the helm. Consequently, changes in the C_M are expected to be mitigated by the automatic control system, minimizing their effect on the vessel's performance.

The airfoil database is firstly skimmed out searching for airfoils described as suitable for hydrofoils. Additional airfoils are included by filtering for a minimum thickness of 10% of its chord, and camber values comprised between 2 and 5 %. Efficiency is assessed by maximising the fraction C_L/C_D, for this reason the results are sorted accordingly.

The following list of candidates are identified and analysed by plotting the C_L, C_D, C_M and C_p plots:

- Eppler 817
- Eppler 818
- Eppler E836
- Eppler E837
- Eppler E838
- Eppler E874
- Eppler E904
- Eppler E908
- YS915
- YS930
- NACA 2408
- NACA 2410
- NACA 2412
- NACA 6409
- GA 30U-615

The Eppler 817 airfoil is identified as the most performing section, especially due to its efficiency peak close to the main foil's cruise speed angle of attack. This is used as a starting point to tune the performance of airfoil to better meet the requirements. Firstly the effect of the following four parameters is assessed: maximum airfoil thickness, position of maximum thickness, maximum camber and position of maximum camber. By also considering the combination of such parameters (23 iterations are produced), a better performing mutation of the E817 with increased thickness (11.46%) and camber (3.48%) is created (noted as airfoil #33). The complete list of studied shapes, as well as additional information of each, is presented in Appendix D.1.1.

This airfoil achieves its efficiency peak at 0.75 C_L with premium performance up to values as low as 0.70 C_L, making it ideal for cruise speed. However, this airfoil shape strongly penalizes the lift-off condition with a C_L/C_D ratio equal to 91, and does not either improve the maximum speed condition with an efficiency of 124.5. For this reason new solutions are searched.

Within the XFLR5 software, two different sections can be fused together in varying proportions to create a hybrid, resulting in a new mutant airfoil shape. Several different mutations are analysed and assessed, using different parent shapes, or different contributions of each airfoil. Airfoils #34 and #48 show potential when fused together with other shapes; after some

iterations, refined candidates are identified. What are believed to be the most performing airfoils are compared in Figure 7.

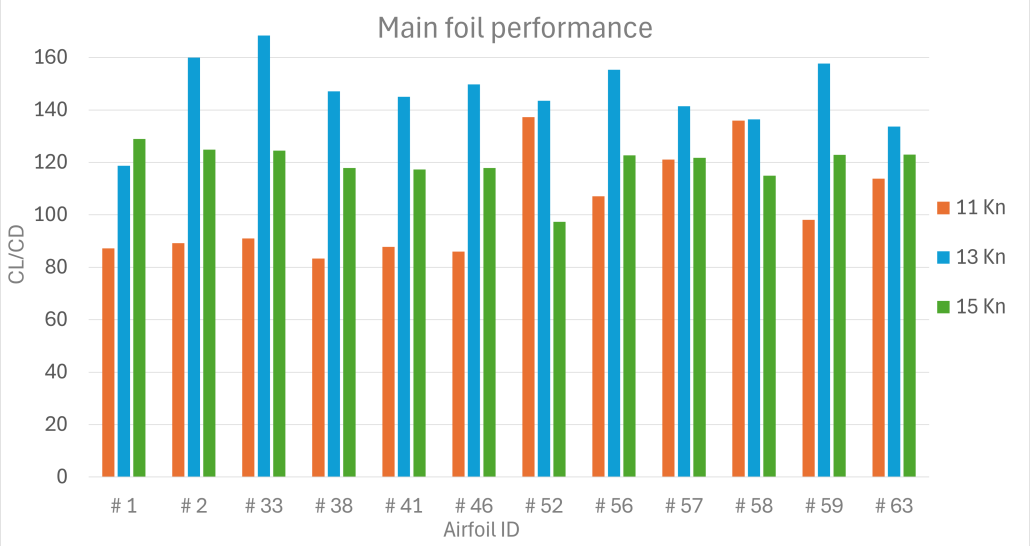

Figure 7: Performance comparison of main foil airfoils

The starting shape, Eppler 817 (noted as airfoil #1), is the airfoil which best performs at high speed, but its low speed efficiency is believed to be insufficient to overcome the water resistance on the hulls allowing the vessel to enter the foiling mode. Airfoil #2, which modifies #1 by increasing the camber, shows significant improvement at cruise speed, but still fails to address the low-speed inefficiencies adequately. This shortcoming limits its ability to transition smoothly from lift-off to flight-cruising. Airfoil #33, identified as the best-performing mutant of airfoil #1, exhibits the highest efficiency at cruise speed, making it optimal for sustained operation at this velocity. Nevertheless, it underperforms at both lift-off and maximum speed, highlighting its limited versatility. Airfoils #38, #41 and #46 are derived from the same parent airfoils, but neither of them improve significantly what airfoil #33 can offer. In addition to this, they have a C_m coefficient which ranges from -0.08 to almost -0.014. Although, as mentioned earlier, C_m is not a crucial parameter that must be considered in this airfoil selection, this large variation could potentially present stability issues when transitioning between flight conditions. Airfoil #52 stands out with very good performance at both lift-off and cruise speed, however what is offered for high speeds is not adequate to suit the purpose. This airfoil produces the necessary amount of lift for larger angles of attack and has a moment coefficient which is smaller in absolute value and presents fewer fluctuations compared to all other candidates. Airfoils #56, #57 and #58 originate from the same parents and demonstrate the impact that the proportion of each ancestor has on the final performance of the airfoil. These shapes show a much more even performance across all conditions, making them versatile options. Lastly, airfoils #59 and #63 show better

efficiency at maximum speed rather than at lift-off speed. This performance profile contradicts the project's objectives, which prioritize high efficiency at both lift-off and cruise speeds to ensure smooth transition into foiling mode and sustained operation.

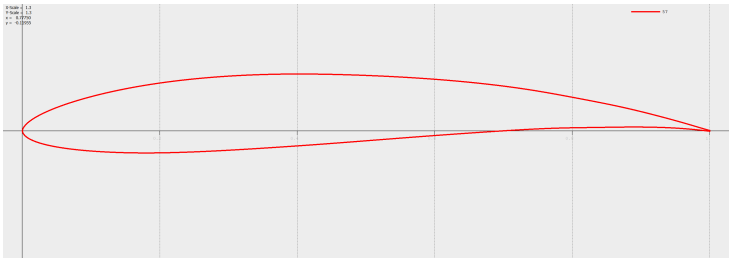

Figure 8: Best performing main foil shape: #57

Based on this analysis, the selected airfoil is #57 (Figure 8) which exhibits a strong performance at cruise speed, without missing out on lift-off nor maximum speed. This airfoil has a moment coefficient which is in the region of -0.138 throughout all operating conditions and reaches a drag coefficient as low as 4.2×10^{-3} at cruise speed. The pressure trough is reached at 20% of the chord length, and is equal to -0.77. Different C_p coefficients for the different conditions are presented in the first two columns of Table 5.

	Kn	Cp	Cavitation margin
Lift-off speed	11	-1,9	2,006
Cruise speed	13	-0,77	2,585
Maximum speed	15	-0,63	2,518

Table 5: Cp troughs for different foiling conditions

It must be verified that the pressure coefficient and the vessel's velocity don't induce cavitation on the foil. This phenomenon occurs when the local pressure on the surface of the hydrofoil drops below the vapor pressure of the water. This leads to the formation of vapor cavities which disrupt the pressure field in the neighbourhood of the wing, causing a significant reduction of efficiency of the wing. The bubbles collapse violently on the surface of the wing, potentially causing impact damage and/or fatigue damage.

Considering the vapour pressure of water at 20°C is 2.34 kPa and that the atmospheric pressure measured at sea level is equal to 101.33 kPa, the local pressure on the airfoil is calculated by flipping the definition of the pressure coefficient C_p:

$$P = P_\infty + C_p \cdot \frac{1}{2}\rho V_\infty^2 \tag{15}$$

It must be noted that P_∞ is increased of the term $\rho g h$ to take into account the water depth. In addition, the second term of the equation is often called dynamic pressure since it depends

on the fluid's velocity. Examining the worst case scenario for all flight conditions and the location of the point under examination (taken at the pressure trough in each scenario), the minimum water depth to avoid cavitation is equal to 0.106 m, which is smaller than the 0.250 m initially proposed in Chapter 3. As can be seen from the last column of Table 5, the cavitation margin λ is defined as:

$$\lambda = \frac{\text{local pressure - vapour pressure of water}}{\text{vapour pressure of water}} \tag{16}$$

λ, is largest at 13 knots, and is the slimmest at lift-off speed, where a higher C_L is needed to overcome low speed. Anyways, at lift-off speed, the wing is fully submerged into the water, meaning that cavitation is never a concern.

At this design stage the central foil and winglets all have the same chosen airfoil shape, but a more detailed design can be achieved by having different sections along the span of the wing. The winglet extremities are structurally less stressed, hence a thinner airfoil section could be used to further reduce drag. A thinner airfoil also typically moves the centre of pressure forward helping the extremities to twist.

9.2 Elevator

The same method seen for the main foil is duplicated once again on the elevator. The objectives and considerations stated in Chapter 9.1 also apply here. The only difference with what was previously said, is that the elevator requires a more constant moment coefficient compared to the main foil. This is because the elevator is controlled by a PID loop, which adjusts the global trim of the vessel by adjusting the elevator angle many times per second. If each change in angle introduces a different pitching moment, then control becomes tedious. For this reason more importance is given to this parameter.

The C_L coefficient required by the elevator foil for each condition are:

	Kn	$C_{L\ 2D}$
Take-off speed	11	0,987
Cruise Speed	13	0,698
Maximum speed	15	0,521

Table 6: Elevator C_L for different conditions

Among all the considered airfoils up to this point, due to its high efficiency peak at small angles of attack, the best elevator candidate is the Eppler E908 profile. Firstly, the effects of varying the same parameters as the earlier analysis are identified. Then, different combinations of camber and thickness on the same shape are also verified. Due to the fact that none of the obtained lead to significant performance improvements, more airfoils are considered in the study.

Particularly the additional elements are:

- A18
- AG 24
- AG 36
- EH 1.0/9.0
- Jukovsky f=0% t=9%
- MH 62 9,3%
- Prandtl-D root
- RoncZ
- PW 51

Several different hybrid combinations of airfoils are created and their performance is evaluated. Out of the resulting 67 tested airfoils, which list is presented in Appendix D.1.2, the most promising ones are shown in the following figure:

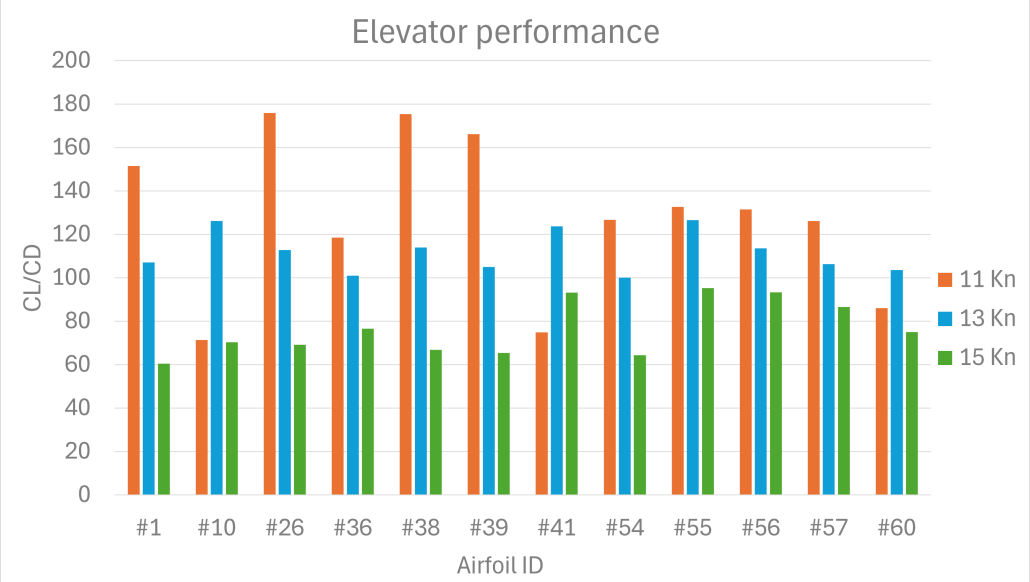

Figure 9: Performance comparison of elevator airfoils

The baseline airfoil, noted as #1, demonstrates the best performance at high lift coefficients, but its efficiency at higher speeds is unsurprisingly small, it is believed to be insufficient to overcome the hull water resistance and achieve foiling mode. Additionally, this airfoil presents a dramatic drop in performance after $C_L = 0.55$, since this condition is very close to the one reached at 11 knots, new solutions are considered. All the airfoils derived from a change in camber and/or thickness of airfoil #1 show the same limitations of the original shape.

As demonstrated with airfoil #10, changing the position where the maximum thickness is found creates an airfoil capable of having its efficiency peak at higher speeds compared to the baseline airfoil. Airfoil #26 is a hybrid of two different promising shapes, but shows significant differences in performance across the three studied conditions, making it less versatile. Airfoil #36 is specifically selected due to its low drag characteristics, but when comparing this shape, others from the list have an overall better performance. Airfoils #38 and #39 are

derived from the two same parent airfoils but with different ratios between them. Similar to #26, both the considered airfoils exhibit significant differences in performance across the three conditions. The best overall performance between all conditions can be noticed when analysing airfoils ranging from #54 to #57. They are all hybrid shapes resulting from the combination of shapes #1 and #30 but with different ratios of each. The ratio influences the C_L/C_D curves for the three speeds, in fact a higher percentage of the baseline airfoil shifts the peak of the curves lower down and at higher angles of attack. Lastly, airfoil #60 presents an even performance across the different conditions, but when comparing this shape with the others in the list, this underperforms. For example airfoils #55, #56 and #57 all show better performance across the whole spectrum than the considered shape.

From all the above considerations, the best performing airfoil is identified as #55. This shape delivers very similar performance at both lift-off and cruise speed (approximately 130), without leaving out maximum speed with an efficiency of little lower than 100. Additionally, this geometry significantly improves the C_M plot compared to the baseline airfoil.

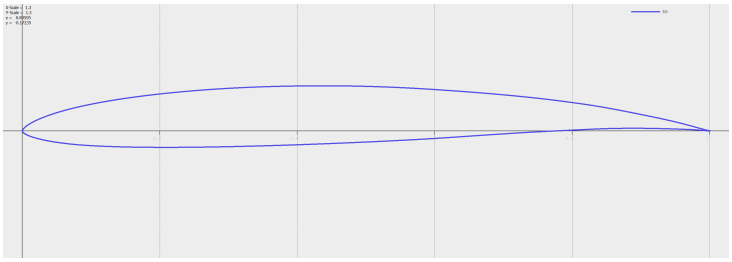

Figure 10: Best performing elevator shape: #55

9.3 Struts

These elements must be as thin as possible to induce the least amount of drag possible, but must be in any case thick enough to support the weight of the vessel out of the water. For this reason a first structural assessment is needed to understand the minimum thickness required by the airfoil. The outcome of the analysis demonstrates that a minimum thickness of 14 mm is required. This result was used to filter out for thicknesses ranging from 14 to 20% of the total chord.

The struts have an influence on the equilibrium of forces and moments when the vessel turns since the latter skids out of corners inducing a leeway angle, which in turn induces an angle of attack on the foils. Since this is valid for both struts, when turning in both directions, the airfoil sections for this purpose must be symmetrical. Moreover, during turns, the struts produce a side force which induce the vessel to bank out of the corner. In this regard it would be best if the struts could produce the least amount of lift and least amount of drag, obviously with the best possible efficiency. Regarding the moment coefficient, this is seeked to be as large as possible to improve turning abilities. The struts and the winglets pointing upwards

help the vessel to remain on course during navigation, for this reason if the struts happen to have a positive C_M (for positive angles of attack), this is believed to help turn the vessel.

All the airfoil sections which are found in the database, that fulfill the requirements listed above, are tested. The complete list of candidates is found in Appendix D.1.3.

Since the behaviour of all shapes is approximately linear, all the airfoils are ranked from best to worse for four categories: Efficiency, Lift, Drag and Moment. The worst ranked airfoil is rewarded with one point, the second worst with two points and so on, until all 20 sections are ranked. The score awarded by every category is then multiplied by a weight factor (the sum of all the weight factors is unitary) and the final ranking is created.

A summary of the performance can be seen in Table 22, which is found in Appendix D.2.

The five most performing airfoil shapes, from best to worst are: #9, #15, #19, #3, #10. Airfoil #9, presented in Figure 11, clearly outperforms all the others by scoring more than 5 points above all other candidates; therefore being the best performing shape.

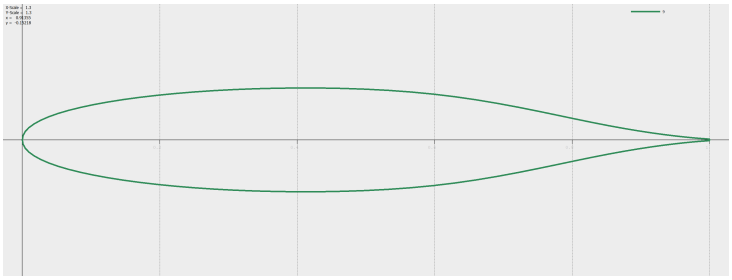

Figure 11: Best performing strut shape: #9

9.4 Rudder

The rudder airfoil shape must be selected taking into account the hydrodynamic requirements needed to steer the vessel during both displacement and flight mode. The rudder must also take into account the structural needs to withstand the loads generated by the elevator.

As the steering requirements are much smaller in flight mode compared to displacement mode, the latter is used as the driving scenario for the rudder sizing. In this regard the rudder shape chosen by the hull and superstructure designer was confirmed after verifying the structural integrity of the element, which will be presented later on in Chapter 11.5.

The confirmed airfoil shape is the NACA airfoil 0021, presented in Figure 12.

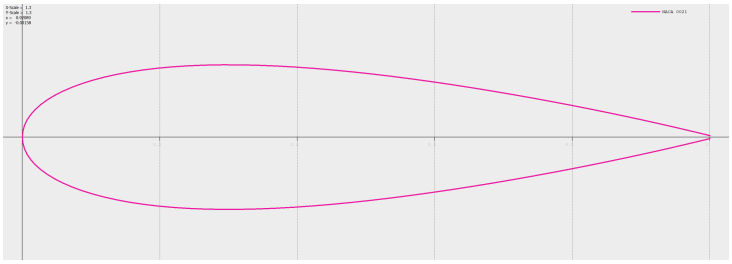

Figure 12: Chosen Rudder shape: NACA 0021

10 Reducing induced drag

To improve the efficiency of the hydrofoil during navigation, different shapes are tested to assess which one produces the least amount of drag for the given amount of lift (i.e., maximising the lift to drag ratio). All the above calculations so far were based on the hydrodynamic loads given by a rectangular shaped 3D wing, this chapter aims to assess the effect of key design details to find the best performing wing shape. The problem is simplified by initially testing different solutions individually to find the optimal feature, and only in a second instance all the best features are recombined to create the optimized foil.

10.1 Methodology

Large flow detachments are not expected to occur due to the small angles of attack, therefore an efficient algorithm such as the k-epsilon model is chosen. This method is capable of capturing flow separation, which is crucial for accurately simulating lift and drag forces. It is a particularly efficient method as it is robust and stable, as it has been validated extensively on external flows with large Reynolds numbers (Khan et al., 2020). A wall function resolves the logarithmic region of the flow close to the no slip walls, where a first layer thickness is imposed. y^+ values for this method are set to 30, hence this value is used together with the flow speed and wing dimensions to determine the first cell size.

All geometries are swept in Rhino 8 starting from fundamental curves, then they are imported into Ansys Workbench using the Design Modeler tool and are eventually discretized into a finite set of elements to approximate the complex designs. All meshes are controlled by adjusting the cell size on the wing and bulb surfaces, as well as on the trailing edge and on the outermost winglet section. The boundary layer is captured by including an inflation zone consisting of 12 layers, which ensures adequate resolution for capturing the near wall effects. The first cell size is set by imposing a y^+ equal to 30, which is required by the used turbulence model. Additionally, bodies of influence are included to further refine the cell size in the neighbourhood of the leading edge and in the wake, dividing the latter into a closer

area which is given a smaller cell size, and a further one with a coarser mesh. According to the tested foil feature, the size of each mesh component is chosen to enhance detail of the flow close to the tested foil feature, always keeping the node count smaller than 500k for smaller and simpler flows, while for more turbulent and larger geometries a limit of 1M nodes is used. This limit is imposed by the Ansys student licence, which restricts the number of nodes available to the user, this constraint requires careful mesh planning to ensure accuracy within the available resources. Throughout all the proposed simulations, symmetry is always exploited to reduce the problems complexity and enhance mesh detail.

Later, all simulations are set up using the CFX Pre tool where the boundary and stopping conditions are defined. A steady fluid velocity of 6.7 m/s is applied at the inlet surface to simulate the hydrofoil travelling at a steady speed of 13 knots on a straight course, while a null average static pressure is set on the outlet surface. The symmetry condition is enforced on the symmetry plane and the free slip condition is applied to the side and bottom boundaries. In contrast, the no slip condition is applied on the surface of the foil and on the top boundary to simulate the effect of the water's free surface. All simulations are stopped once the residuals converge to values smaller than 10^{-6}, to ensure high accuracy results. If this requirement is not met, simulations are capped at a maximum of 200 iterations.

After each simulation, the results are post processed using the CFX Post tool. This includes obtaining forces along all principal directions and collecting pressure and velocity distributions on and near the foil.

10.2 Testing different designs

Induced drag is reduced by avoiding the formation of stagnation zones and minimizing vortex formation at the winglet extremities, which can be achieved using wing tips. Additionally, induced drag is proportional to how the pressure distribution changes along the span of the wing and can be reduced by considering the use of wing tips. The latter are small, fin-like vertical or angled extensions at the extremities of the wings, which work by diffusing the wingtip vortices, thereby reducing the strength of the vortices and consequently the induced drag. An evenly distributed pressure along the span of the airfoil improves efficiency, but can lead to simultaneous stalling across the span at higher angles of attack. As stated in Chapter 3, stalling characteristics are believed not to influence the design as the vessel will operate for a limited range of trim values, therefore, the primary design focus remains on optimizing the lift to drag ratio and minimizing induced drag.

Tables ranging from 7 to 12 show the summary for every step of the analysis. The mesh column represents the node count divided by 1000, while the lift and drag columns represent the forces in Newtons generated along the Z and X directions respectively. The best analysed solution is chosen for the maximum lift to drag ratio.

10.2.1 Winglet planform shape

Firstly, the winglet seen from a top view is assessed. Winglet shapes are constructed by using the sweep feature between the airfoil sections, presented in Chapter 9, and rails which delimit the hydrofoil boundary. The airfoil section at the extremity of the wing is reduced to 30% of the root dimension.

Figure 13 shows the different winglet planform shapes which are tested.

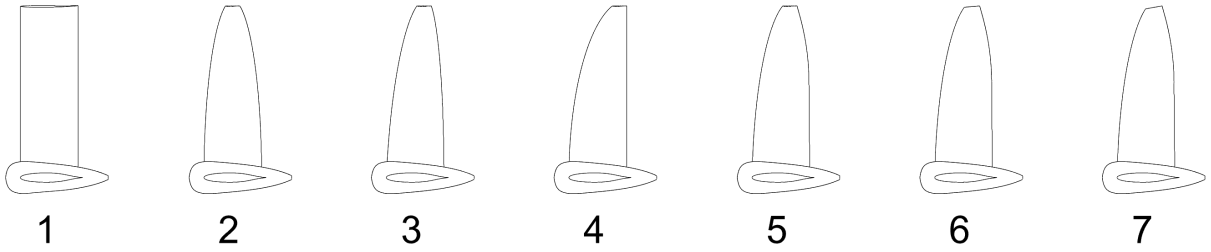

Figure 13: Tested planform shapes geometries

Geometry number 1 shows a rectangular shaped winglet, while in geometry number 2 the rails become elliptical. Geometry number 3 is similar to the second proposed geometry, with the winglet tip translated aft by 50 mm. Geometry 4 has a flat trailing edge with an elliptical leading edge. Lastly geometries from 5 to 7 show a semi elliptical wing with a tapered trailing edge. Geometry 5 has a straight winglet tip, geometries 6 and 7 show a winglet tip which is respectively rotated by 5 and 10 degrees. Since the tested feature is the winglet planform area, the mesh detail is emphasised on the leading edge, on the winglet extremity and in the wake areas.

ID	**Geometry**	**Mesh**	**Convergence**	**Lift**	**Drag**	**L/D**
1	Rectangular planform	956	10^{-6} in 183 iter. 46 min	3,75E+03	2,45E+02	15,34
2	Elliptical planform	952	10^{-6} in 142 iter. 34 min	3,21E+03	1,64E+02	19,63
3	Elliptical swept back	994	10^{-6} in 176 iter. 43 min	2,76E+03	1,73E+02	15,95
4	Flat TE	867	10^{-6} in 151 iter. 37 min	2,83E+03	1,70E+02	16,65
5	Semi elliptical	981	10^{-6} in 158 iter. 39 min	3,28E+03	2,01E+02	16,28
6	Semi elliptical 5 deg	987	10^{-6} in 156 iter. 39 min	3,27E+03	2,02E+02	16,22
7	Semi elliptical 10 deg	921	10^{-6} in 158 iter. 40 min	3,28E+03	2,02E+02	16,24

Table 7: Winglet planform simulation summary

The most efficient planform shape is, as expected, the elliptical wing which produces an outstanding lift to drag ratio and an even pressure distribution along the whole span of the wing. Also planform n4 described by a flat trailing edge performs strongly with a ratio equal to 16.65.

10.2.2 Transverse section

Instead of having a straight leading and trailing edges, a curved geometry is tested. As shown in Chapter 8, foils pointing upwards enhance lateral stability and for this reason, this design possibility is verified.

Figure 14 shows the different transverse section shapes which are tested.

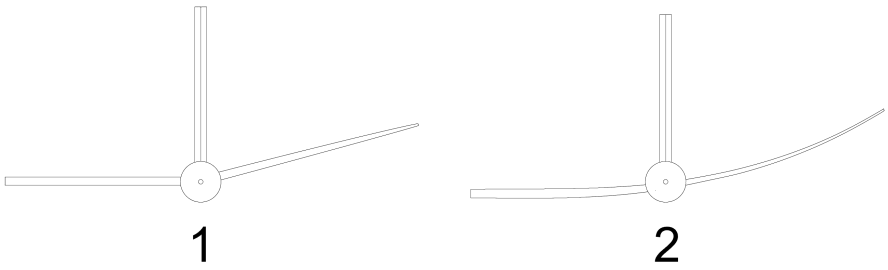

Figure 14: Tested transverse section geometries

Geometry 1 is characterized by a straight leading and trailing edges, while geometry 2 has curved edges.

ID	Geometry	Mesh	Convergence	Lift	Drag	L/D
1	Sharp edge	972	10^{-6} in 117 iter. 29 min	7,09E+03	3,19E+02	22,21
2	Rounded edge	776	10^{-6} in 120 iter. 22 min	6,57E+03	3,19E+02	20,59

Table 8: Transversal sections simulation summary

The potential improvement in lateral stability only during turns does not justify the $7,4\%$ decrease in efficiency. For this reason, geometry number 1 is preferred.

10.2.3 Tip shape

To reduce slippage at the wing extremity, different tip shapes are assessed. All the different geometries are tested on the same winglet shape (n3) to evenly compare the results. All winglets are obtained by further reducing the tip extremity, by rotating and by translating it.

Figure 15 shows the different tip shapes which are tested.

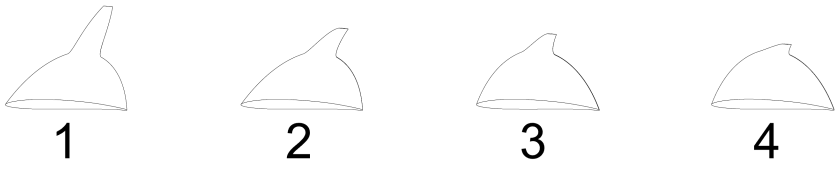

Figure 15: Tested tip geometries

Geometry 1 shows the tip extremity which is translated 100 mm aft and 50 mm for increasing Y and Z directions, this results in a large tip. Geometry 2 shows a similar configuration, this time the extremity is translated by 50 mm, resulting in a medium sized winglet. Geometries 3 and 4 instead show smaller winglets, respectively a small and extra small winglet. All tip extremities are rotated 75 degrees with respect to the horizontal axis.

ID	Geometry	Mesh	Convergence	Lift	Drag	L/D
1	Large	902	10^{-6} in 104 iter. 20 min	6,40E+02	4,12E+01	15,54
2	Medium	609	10^{-6} in 91 iter. 18 min	7,50E+02	4,37E+01	17,18
3	Small	419	10^{-6} in 70 iter. 14 min	7,41E+02	4,09E+01	18,12
4	Extra small	498	10^{-6} in 160 iter. 27 min	7,31E+02	4,10E+01	17,80

Table 9: Tips simulation summary

The tip which best impedes the flow to orbit around the wing extremity from the pressure peak (measured on the lower surface of the wing) to the pressure trough (measured on the upper surface) is winglet 3, which is the small tip.

10.2.4 Tip for winglet

After determining that tip 3 was the most effective, it was tested by attaching it to the most efficient winglet planform shapes presented in Chapter 10.2.1 (Geometries 3 to 5).

Geometry 1 is generated by merging tip 3 together with winglet 3; geometry 2 is generated by merging tip 3 together with winglet 4 and geometry 2 is generated by merging tip 3 together with winglet 5.

ID	Geometry	Mesh	Convergence	Lift	Drag	L/D
1	Tip 3, winglet 3	964	10^{-5} in 200 iter. 26 min	3,39E+03	1,67E+02	20,23
2	Tip 3, winglet 4	496	10^{-5} in 200 iter. 28 min	3,37E+03	1,70E+02	19.89
3	Tip 3, winglet 5	948	10^{-5} in 200 iter. 27 min	2,86E+03	1,65E+02	17,35

Table 10: Tip for winglet simulation summary

The most performing set of planform shape and winglet are tip 2 and winglet 3. By comparing the lift to drag ratio in this scenario, with the ratio given for a winglet with no tip, including the tip creates a 3,2% increase in performance. For this reason the tip is included in the definitive design.

10.2.5 Bulbs

The intersections between the vertical struts and horizontal main foil must host the electrical motors, for this reason different bulb geometries are tested. At this stage of the design no

particular engine is selected, but a clearance equal to a cylinder with a base of 150 mm of diameter, and a length of 400 mm is believed to be required. Two slender and two wider bulb heads and bulb tails are created. The four tested geometries are the possible combinations of the proposed bulb heads and tails.

Figure 16 shows the different bulb shapes which are tested.

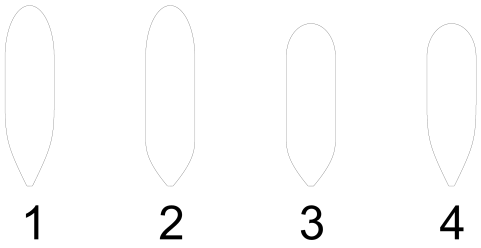

Figure 16: Tested bulb geometries

Geometry 1 is given by merging a thin head with a thin tail; geometry 2 is given by merging a thin head with a thick tail; geometry 3 is given by merging a thick head with a thick tail; lastly geometry 4 is given by merging a thick head with a thin tail.

ID	**Geometry**	**Mesh**	**Convergence**	**Drag**
1	Thin head, thin tail	448	10^{-6} in 75 iterations. 22 min	1,47E-02
2	Thin head, thick tail	477	10^{-6} in 99 iterations. 30 min	1,86E-02
3	Thick head, thick tail	433	10^{-6} in 95 iterations. 28 min	1,81E-02
4	Thick head, thin tail	434	10^{-6} in 74 iterations. 25 min	1,42E-02

Table 11: Bulbs simulation summary

The bulb shape which creates the least amount of drag for the required internal volume to host an electric motor is bulb 4, the one with a thick head and a thin tail.

10.2.6 Rudder transverse section

The planform shape to be used on the rudder was already tested in Chapter 10.2.1 when analysing the different winglet solutions. As seen in the previous study, elliptical wings are the most efficient planform shapes. The rudder will be produced using a machined closed mould, hence even a complex surface with a double curvature such as an ellipsoid should not push the change in geometry of an efficient planform shape. All geometries are created with an extremity airfoil section which is 30% smaller than the root airfoil dimension. A very small bulb is included in the intersection between the vertical rudder blade and the elevator to better blend the intersection.

To complete the rudder shape, different transversal sections are addressed. Figure 17 shows the different geometries which are tested.

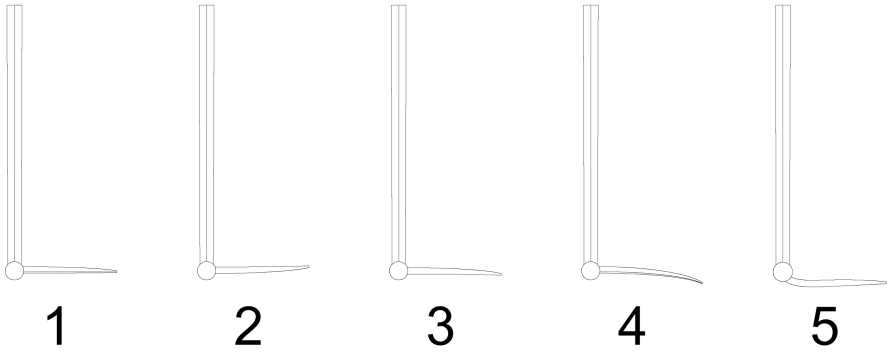

Figure 17: Tested rudder transverse section geometries

Geometry 1 is given by rudder extremity which is positioned amid of the root, resulting in an elevator which is exactly horizontal along the mid surface of the elevator. The rudder extremity on geometry 2 is translated upwards, so that the upper surface between the root and the extremity is horizontal. Consequently geometry 3 is similar to the just introduced elevator, but in this case the lower surface of the root and of the extremity are aligned. Lastly geometries 4 and 5 show both the elevator extremity lowered by 50 mm, but the first shows a large curvature close to the extremity, while the second has the large curvature close to the elevator root.

ID	**Geometry**	**Mesh**	**Convergence**	**Lift [N]**	**Drag [N]**	**L/D**
1	Tip amid root	459	10^{-5} in 200 iter. 61 min	5,44E+02	1,08E+02	5,04
2	Tip above root	457	10^{-5} in 200 iter. 60 min	4,76E+02	1,07E+02	4,44
3	Tip below root	475	10^{-5} in 200 iter. 58 min	4,74E+02	1,05E+02	4,51
4	Curved near tip	499	10^{-5} in 200 iter. 31 min	4,70E+02	1,04E+02	4,51
5	Curved near root	486	10^{-5} in 200 iter. 31 min	4,68E+02	1,05E+02	4,48

Table 12: Rudder transverse section simulation summary

The most efficient rudder shape is the simplest geometry between the tested range: geometry 1. In this condition low slippage from the top to the bottom surface is generated.

10.3 Optimized design

Given the multitude of details tested in this chapter, the most performing geometry for each tested feature is used to create what is considered to be the best performing foil shape. This geometry is composed of:

1. Main Foil
    - **Planform shape:** number 3
    - **Transverse section**: number 1
    - **Tip shape:** number 3
    - **Bulb:** number 3
2. Rudder
    - **Planform shape:** number 2
    - **Transverse section:** number 1

The proposed design is characterized by the following lift and drag coefficients. Table 13 presents the performance of the optimized design against the starting rectangular geometry. By comparing the results, a total of 51% and 24% increase in performance on the main foil and rudder is respectively noticed.

		Lift [N]	**Drag [N]**	**L/D**
Original geometry	**Main foil**	3,77E+03	2,45E+02	15,42
	Rudder	5,33E+02	1,32E+02	4,05
Improved design	**Main foil**	7,65E+03	3,28E+02	23,29
	Rudder	5,44E+02	1,08E+02	5,04

Table 13: Performance of the optimized design against the starting geometry

11 Structure

To ensure structural integrity, the loads presented in Chapter 4 and the optimized geometry for drag reduction presented in Chapter 10.3 are used to perform the structural assessment.

Different construction strategies can be used to produce the studied component. A metallic foil can be easier to produce, simply by loading the material onto a CNC machine, which can be then mechanically processed with a 5 axis milling head, first on one side and then on the opposite surface. This would also ease the connection between the horizontal main foil and the vertical strut, this can be made by bolting the two milled pieces together. However, this choice is costly and requires a large quantity of raw material, which would be discarded during the manufacturing process. Alternatively, the hydrofoil can be milled starting from a unique block of material, but this would inevitably affect even more the cost of the required resources. Also, a mechanical processing machine with a large working volume must be used, which is not accessible by many shipyards. By choosing a metallic material, the produced artefact would

be traditional, where the behaviour is isotropic and the shape deforms equally in all directions. Different structural behaviours could be induced by changing the foil geometry, at the expense of changing the initial hydrodynamic performance. This would result in a hydrofoil which cannot be tuned to better suit the requirements imposed by problem, without changing the structural and hydrodynamic behaviour simultaneously.

Since the project consists in testing and exploring new solutions to the hydrofoiling vessel problem, a composite wing is preferred to better unfold new opportunities. An asymmetric lamination plan can be used to induce flexing and twisting along the span of the foil, which effects can be used to improve rolling abilities or efficiency. Although the vertical struts are mostly loaded in compression and for this load case, composite materials are not exploited at their most, these elements are also produced in the same way as the main foil to give continuity to the production process and to ease the connection between the vertical and the horizontal elements, which otherwise would require a more complex assembly and engineering of the design. Pairing materials with different mechanical properties can lead to uneven load, stiffness and stress distributions, breeding to potential failure points. Galvanic corrosion is also a concern because an exposure of the metal to moisture, which is inevitable in a marine environment, will lead to the degradation of the metal. Additionally, this choice would also lead to maintenance challenges, such as the need for specialized workforce in both branches of composite and metallic structures and the need of equipment for the inspection of both materials. For these reasons, the structure is completely sized using composite materials.

The goal of the structural design is to ensure structural integrity during any condition the vessel might face throughout its lifetime. In this regard safety on board must be guaranteed in any scenario.

As was presented earlier, rolling abilities are the ones which concern the most, for this reasons, Chapter 8 proved that the more the tips are pointing upwards, the more stable the vessel becomes. In particular, the recalled chapter emphasises the fact that during turns, the outer wing should produce more lift than the inner one in order to compensate the force generated by the struts, which tends to bank the vessel out of the corner when the vessel is drifting. For this reason, the structure is desired to firstly twist, which in turn will allow the winglet to flex. If the design goal would have been to firstly bend, no twisting could have been induced, while by following the opposite sequence, a stronger effect can be reached. Twisting on the winglet induces a larger AoA with respect to the flow, which in turn increases the hydrodynamic load generated by the section, which leads to a larger bending of the winglet. Additionally, when turning, the stability spreadsheet demonstrates that the outer winglet has a larger AoA compared to the inner foil, moreover the inner winglet travels a shorter distance compared to the outer foil. For these reasons, and since lift is directly proportional to the square of the fluid velocity, the outer winglet produces a larger lift. To improve the rolling abilities when turning, the composite stacking sequence must take advantage of the larger load on the outer wing to flex and twist more, compared to the inner winglet.

During the analysis, several different solutions are assessed, ranging from the use of different

types of glass and of carbon, as well as the use of different resins. At this stage of the design, generic material properties found in text books are used, instead of ones derived from industrial data sheets.

11.1 Analytic method

'Classical' solid mechanics theory is used to address the loads acting on the system: on all structural members, forces are perpendicular to the wings producing bending moments. On the other hand, the struts and the rudder experience, in addition to a bending moment, also compressive stresses, leading to potential buckling issues. Sophisticated simulation tools should be used to address the non linear nature of the buckling phenomenon, but at this stage of the design, this problem will be solved as the linear combination of each single effect. It must be highlighted that awareness should be put during the scrutiny of these results, since buckling is a highly non-linear phenomenon.

Once the loads are identified, the lamination ply book is drafted by means of the Classical lamination theory, and the results are validated with a more complete FEA analysis using Solidworks.

11.2 Materials selection

In order to assess the structural integrity of the hydrofoil, suitable materials are identified which can fulfill the requirements, remaining within the given constraints. This process involves creating a material index, and using it to assess various opportunities to find the optimal combination that satisfies all the requirements and constraints.

The primary objectives of the materials are to achieve high rigidity on the central foil to minimize deflection, while ensuring significant flexibility on the outer winglets to allow controlled flexing without breaking. Especially on the winglet, long-term durability (fatigue resistance) must be provided. In addition, for both main foil and rudder, the additional objective is to have resistance to seawater corrosion, reduce the overall mass of the wing to enhance performance and ease manufacturing and assembly.

Several constraints must be considered in the selection process: the assembly will operate within a temperature range of 5-40°C and will be exposed to seawater salinity. The manufacturing process will involve vacuum infusion or autoclave curing thanks to its ease of manufacturing complex shapes, and requiring materials that exhibit strong adhesion and durability in a marine environment. Moreover, there are non-mandatory limitations that could be added to improve wing performance and maintainability, such as impact resistance to provide it with endurance against potential impacts with debris and to ease repair in the event of damage.

Considering the just introduced objectives and constraints, by cross-matching the deflection for a beam fixed on its two ends with the mass of the same beam (since the geometry is fixed),

the following material index is created:

$$m = \left(\frac{12\ S\ L^3}{C}\right)^2 \cdot L \cdot \left(\frac{\rho}{E^{1/2}}\right) \tag{17}$$

By maximising the last term of Equation 17, which is the addend which depends uniquely on the material properties of the beam, into an Ashby diagram, the appropriate material found for a stiff beam is a carbon composite, in particular a high strength fiber is chosen which offers superior stiffness and minimal deflection under load; this material is chosen for the central foil, the rudder and the vertical struts. Where instead deflection is needed, glass fiber is preferred to carbon thanks to its lower rigidity. Although other materials could have been considered more thoroughly, the choice of composite is mandatory to give continuity to the design. The chosen glass fiber is the E-glass, this provides the best strength properties, together with fatigue resistance characteristics. The resin which is chosen to support both fabrics is epoxy, which provides strong adhesion, durability, and resistance to seawater corrosion, ensuring long term reliability and structural integrity in the marine environment. The list of mechanical properties of the materials are found in Appendix E.

To limit the purchase of many different fabric types and fabric weights and optimize the supply chain, only 500 g/m^2 and 1500 g/m^2 of uni-directional fabric rolls are used. If glass UD is not available, this could be replaced with a bidirectional fabric, which is more likely to be available on the market.

11.3 Solid Mechanics Theory

11.3.1 Main foil & Elevator

In order to appropriately quantify the loads acting on the system, the complete problem is first simplified as if the winglets are an extension of the central foil. Each section of the foil is modelled as a simple beam, and the problem is further simplified by using only half of the foil. Boundary conditions are then applied with a roller support as a replacement of the strut connection to constrain the vertical displacement, and a guided support is positioned in proximity to the symmetry plane to constrain rotation and horizontal displacement. In this way, the problem is statically determined as the degrees of freedom of the system are fully controlled by the constraints. For ease of calculation, the load distribution is simplified to be constant throughout the span of each element, hence the load F_1 applied on the cantilever section, is replaced with a constant distribution q_1, while load F_2 which acts on the inner portion, is replaced with q_2.

Figure 18 shows the complete problem, and how this is simplified by including the symmetry condition, the boundary conditions and the constant loads. Lastly also the reaction forces are included.

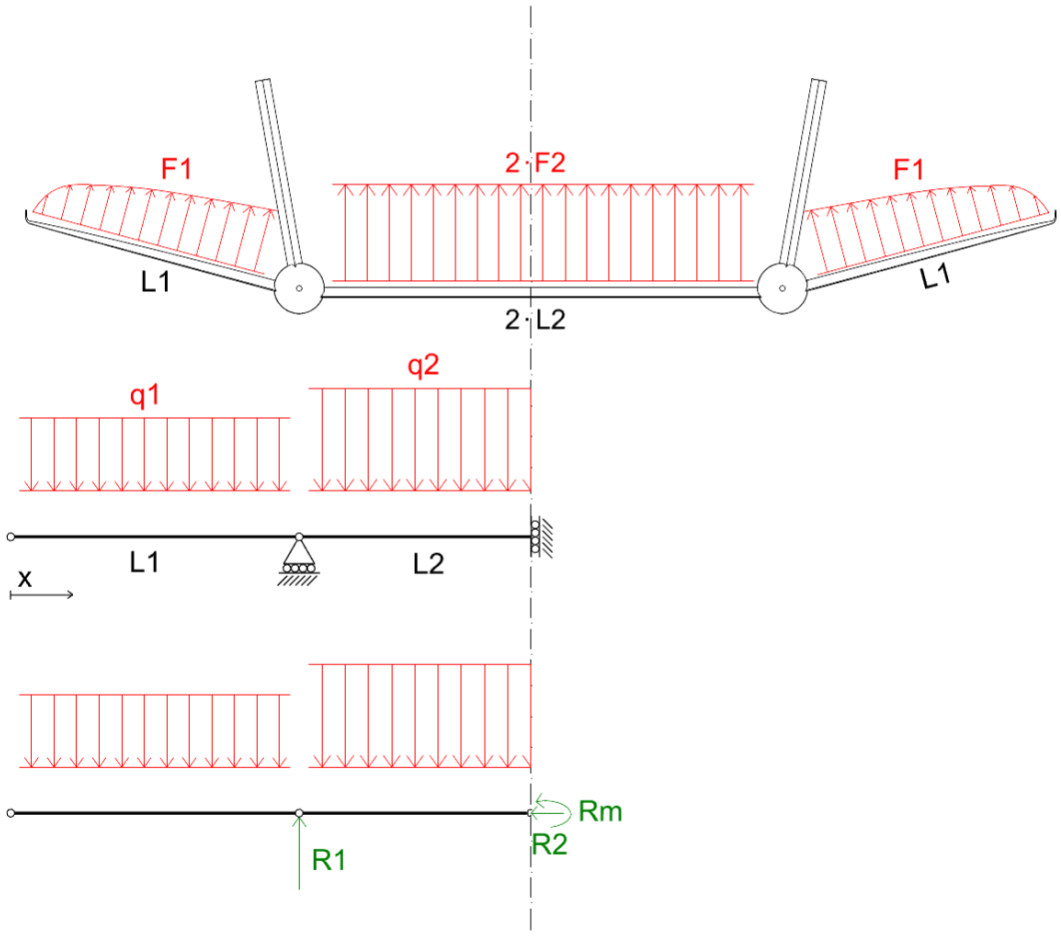

Figure 18: Structural problem presentation and schematic simplification

A summary of the forces action on each section are found in the following table:

	port winglet	**central foil**	**stbd winglet**		**strut**	**elevator**	
Lift (z)	-3477	-8566	-3477	**N**	0	-2750	**N**
Drag (x)	-629	-1712	-629	**N**	-16	-239	**N**
Side F. (y)	620	0	-620	**N**	0	0	**N**

Table 14: Steady state forces generated by the hydrofoil

Since these are the steady state forces, the results are multiplied by a dynamic factor, set as the industry standard, equal to 3.5.

Firstly the main foil is assessed. The reaction forces are obtained by ensuring the equilibrium

of forces and moments on the whole system:

$$\begin{cases} R_1 = q_1 \cdot L_1 + q_2 \cdot L_2 \\ R_2 = 0 \\ R_m = \frac{q_1 \cdot L_1^2}{2} - \frac{q_2 \cdot L_2^2}{2} \end{cases} \tag{18}$$

Then, the shear on the first section is obtained in the local system aligned with the length of the beam, hence the bending moment is obtained by integrating the obtained result.

$$T_1(x) = -q_1 \cdot x; \qquad M_1(x) = -q_1 \cdot x^2 \tag{19}$$

The same result is calculated again on the second section. The difference with the previous case is that in this scenario, since the beam is continuous with the first section, the bending moment induced in the first section is transferred to the second one. This is used as a boundary condition when integrating the shear load.

$$T_2(x) = q_2 \cdot (L_2 - x) \qquad M_2(x) = q_2 \cdot x \left(\frac{x}{2} - L_2\right) + \frac{q_1 \cdot L_1^2}{2} \tag{20}$$

The bending moment acting on the rudder elevator is calculated using the same method, in particular Equation 19 is used since this section is modelled as a cantilever beam, as seen for the winglet on the main foil.

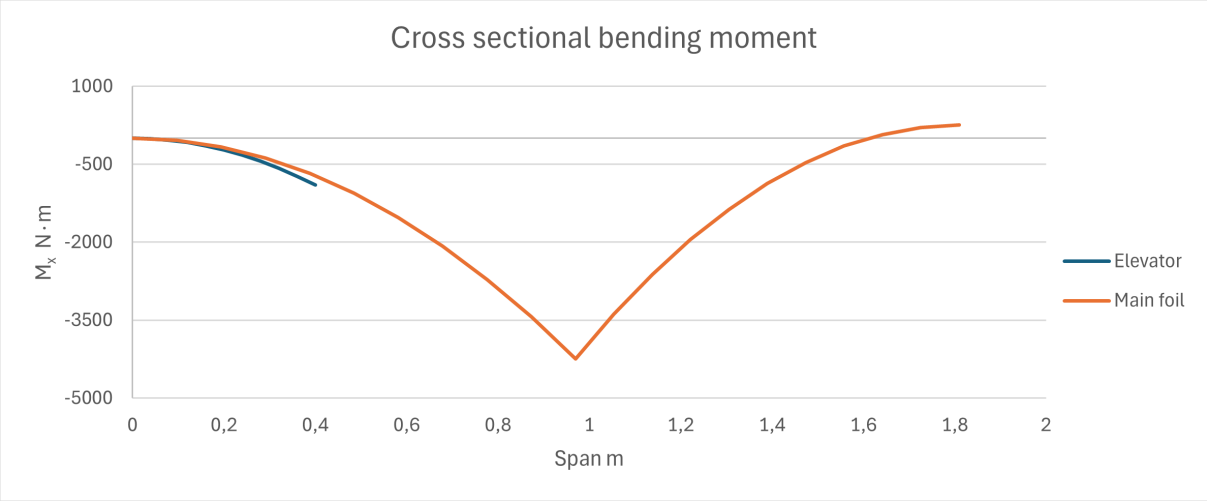

Figure 19: Cross sectional bending moment on main foil and elevator

As can be seen in Figure 19, for this particular set of loads acting on the structure, the most stressed main foil section is reached on the strut connection close to the pinned support and is equal to $-4.5\ kN \cdot m$. The bending moment then increases when travelling in both direction, away from the strut. On the winglet extremity the moment is null, as expected,

while on the opposite side, in proximity of the symmetry plane, the bending moment reached is 253 $N \cdot m$. For larger loads (P_2 in Equation 20) the resulting bending moment in proximity of the symmetry plane would have been larger. In fact, as the just recalled equation suggests, the curve is a concave parabola with its peak at amid of the central section of the central foil. In this explanation the structure was modelled with horizontal winglets. Instead, in the case of angled winglets, the vertical component of the applied load transferred to the central section is smaller, resulting in a less alarming scenario. At the same time, the horizontal component of the lift generated on the winglets creates a compressive state on the central section of the main foil. At 15 deg the compressive force on the central foil is equal to 2.7 kN (taken a safety factor of 3.5) on each side, and if the lift force is considered simultaneously, the result is that the central foil bends more and the strut connection rotates outwards pushing the winglet downwards. This effect could be mitigated by creating stiff struts and central foil. In this regard, both the critical loads were used as an external load on the structure: compression on the central foil and maximum bending moment caused by the winglet load to be in the worst case scenario. Examining further Figure 19, the curve's concavity suggests that the fibers along the lower part of the material are loaded for almost the whole length of the structure in tension, while the upper fibers are loaded in compression.

Being the elevator supported only on one extremity, as a cantilever beam, the most stressed point is located, as expected, in the junction between the elevator and the rudder blade and is equal to -1 $kN \cdot m$. The same considerations on the beam's concavity and fiber placement introduced for the main foil, apply also for the rudder.

11.3.2 Struts & Rudder

The vertical sections of the structure are subjected both to compression and to bending. While not particularly rigorous, the analysis simplifies the effect of the two loads by addressing them individually.

Buckling is assessed using the Euler buckling theory which identifies a critical load above which the column will buckle. Its formula is presented in Equation 21. This is a simplified method which guarantees that global buckling does not occur. At further stages of the design process, a more detailed buckling analysis should be done to avert any local buckling.

$$W_E = k^{-1} * \frac{\pi^2 EI}{L^2} \tag{21}$$

Where k is the buckling coefficient, which takes into account the boundary conditions. In this case, since the design of the connection between the struts and the keel is outside the scope of this work, a conservative approach is used imagining the support on the under side keel to be fixed and the connection close to the main foil to be free. The elastic modulus E which is used in the above equation is the modulus of the whole lamina along the vertical direction of the strut. This is calculated as the inverse of the element found in position 11 of the compliance matrix, which will be explained more extensively in the following chapter.

Equation 21 is applied once again on the rudder foil to assess its buckling integrity.

Instead, the bending of the struts and rudder is studied with the same method as presented in the previous chapter. The same boundary conditions used for the buckling analysis are used once again, resulting in a linear bending moment with its maximum located in the connection between the vertical and horizontal elements.

A summary of the buckling critical loads and the induced bending moments of the vertical sections of the hydrofoil are summarized in Table 15.

	Strut	**Rudder**	
Buckling critical load	12475	11521	**N**
Max bending moment	11625	24500	**N·m**

Table 15: Summary of loads on vertical struts

11.4 Composite stacking sequence

The composite stacking sequence is identified using the Classical Lamination Theory, which is based on the following hypothesis.

- Each lamina is orthotropic,
- Each lamina is homogeneous,
- Any section which is perpendicular to the mid surface of the laminate remains so for any deformation of the laminate,
- The laminate is thin and is loaded only in its plane,
- Each lamina is elastic,
- No slip occurs between each lamina interface.

With these hypotheses, the stress variation for each ply is linear, while the stress distribution shows some abrupt changes. The material properties of the matrix and the reinforcements are used to calculate important quantities such as weight fraction and volume fraction of both materials, the lamina thickness, lamina density, and equivalent Young modulus, shear modulus and Poisson's ratio.

This data is necessary to find the reduced stiffness matrix [Q] for each ply, which relates the stresses to the deformations.

$$\begin{bmatrix} \sigma_1 \\ \sigma_2 \\ \tau_{12} \end{bmatrix} = \begin{bmatrix} Q_{11} & Q_{12} & 0 \\ Q_{12} & Q_{22} & 0 \\ 0 & 0 & Q_{66} \end{bmatrix} \begin{bmatrix} \varepsilon_1 \\ \varepsilon_2 \\ \gamma_{12} \end{bmatrix} \tag{22}$$

where

$$Q_{11} = \frac{E_{11}}{1 - \nu_{12}\nu_{21}} \tag{23}$$

$$Q_{12} = \frac{\nu_{21}E_{22}}{1 - \nu_{12}\nu_{21}} \tag{24}$$

$$Q_{22} = \frac{E_{22}}{1 - \nu_{12}\nu_{21}} \tag{25}$$

$$Q_{66} = G_{12} \tag{26}$$

Equation 22 is then rotated of an angle ϕ to account for any ply orientation angle by multiplying Q by a rotation matrix, this leads to the $\overline{Q}$ matrix. The coordinates of the top, mid and bottom of each lamina are identified and the distance of each point is calculated from the neutral axis. Once $\overline{Q}$ and the positions of each ply are identified, three matrices A, B and D are calculated, hence the compliance matrix is found.

$$\begin{bmatrix} N_x \\ N_y \\ N_{xy} \\ M_x \\ M_y \\ M_{xy} \end{bmatrix} = \begin{bmatrix} A_{11} & A_{12} & A_{16} & B_{11} & B_{12} & B_{16} \\ A_{12} & A_{22} & A_{26} & B_{12} & B_{22} & B_{26} \\ A_{16} & A_{26} & A_{66} & B_{16} & B_{26} & B_{66} \\ B_{11} & B_{12} & B_{16} & D_{11} & D_{12} & D_{16} \\ B_{12} & B_{22} & B_{26} & D_{12} & D_{22} & D_{26} \\ B_{16} & B_{26} & B_{66} & D_{16} & D_{26} & D_{66} \end{bmatrix} \begin{bmatrix} \varepsilon_x^0 \\ \varepsilon_y^0 \\ \gamma_{xy}^0 \\ \kappa_x \\ \kappa_y \\ \kappa_{xy} \end{bmatrix} \tag{27}$$

with

$$A_{ij} = \sum_{k=1}^{n} Q_{ijk}(h_k - h_{k-1}) \qquad \text{with } i = 1, 2, 6 \text{ and } j = 1, 2, 6 \tag{5a}$$

$$B_{ij} = \frac{1}{2}\sum_{k=1}^{n} Q_{ijk}(h_k^2 - h_{k-1}^2) \qquad \text{with } i = 1, 2, 6 \text{ and } j = 1, 2, 6 \tag{5b}$$

$$D_{ij} = \frac{1}{3}\sum_{k=1}^{n} Q_{ijk}(h_k^3 - h_{k-1}^3) \qquad \text{with } i = 1, 2, 6 \text{ and } j = 1, 2, 6 \tag{5c}$$

If the external loads are known, the generic elastic response of the laminate is calculated.

There results are in turn used to calculate the strain and stress in each ply in both the global and local systems. The global deformation of any lamina is written as:

$$\begin{Bmatrix} \varepsilon_x \\ \varepsilon_y \\ \gamma_{xy} \end{Bmatrix} = \begin{Bmatrix} \varepsilon_x^0 \\ \varepsilon_y^0 \\ \gamma_{xy}^0 \end{Bmatrix} + z \begin{Bmatrix} \kappa_x \\ \kappa_y \\ \kappa_{xy} \end{Bmatrix} \tag{29}$$

While the global stresses are found using the $\overline{Q}$ relationship introduced earlier. Results in the local frame are obtained by multiplying the global stress or strain values by the transformation matrices.

Stresses are then input inside the Tsai-Wu criterion to assess the structural integrity of the structure. This criterion is suitable when material properties and strengths in different directions are considerably different, leading to a more accurate prediction of failure for anisotropic materials. This criteria is considered the most conservative and reliable for complex stress states such as this one.

The technique presented in this chapter can provide guidance to assess the orthotropic behaviour of the laminate under a particular load, but it must be noted that some rough assumptions are made by doing so. This tool is used to evaluate the response of the stacking sequence, while a more quantitative analysis is done by performing an FEA analysis of the problem.

The structure is designed to be built in a two sided split mould using the vacuum infusion process. A high quality industrial standard fiber content using this process is 55%, hence $V_f = 50\%$ is used as safe judgement (Hammami, 2000). All the components are built starting off of a split mould and the layers are applied one by one. In areas where the airfoil thickness is smaller than the stacking sequence thickness, the plies must be trimmed of starting from the ones closer to the neutral axis. Alternatively, areas which are thicker than the airfoil thickness (close to the mid chord) are fitted with a PVC foam to further enhance the airfoil's performance. To avoid any exothermic reaction during the cure phase, the stacking sequence is completed in multiple steps, making sure the resin has fully cured after each step.

11.4.1 Main foil & Elevator

The best bending rigidity is achieved by applying numerous fibers along the length of the foil. This direction is designated as the zero direction for the stack up frame, with increasing angles for anticlockwise rotations. This goal is better achieved by creating a symmetric stacking sequence.

In this ply lay-up, the bending-twisting terms B_{16} and B_{26} of the compliance matrix are zero, indicating no coupling between bending loads and twisting displacements, and vice versa. After several attempts and iterations, a total of 48 plies, mostly laid along the span of the wing, are used resulting in a total maximum thickness equal to 38.76 mm. The remaining laminas are laid at $\pm 45^\circ$ with just four plies of perpendicular reinforcement close to the neutral axis. Given the symmetric nature of the stacking sequence, only half of it is presented in Table 16.

Ply n°	1	2	3-4	5-10	11-12	13-14	15-18	19-20	21-22	23-24
g/mm^2	500	500	500	1500	1500	500	1500	1500	500	1500
orientation	45	-45	0	0	-45	0	0	45	0	90

Table 16: Central foil semi stacking sequence

Alternatively, the winglets are desired to have extremities which are able to flex and twist.

More in particular a twisting winglet is preferred over a bending one since a twisting foil can change its angle of attack creating more lift force, which in turn will further bend the wing. If bending would have been preferred, this wouldn't have had any influence on the twisting of the airfoil. The first option is preferred over the second one to enhance the rolling abilities of the vessel during a turn. This is achieved on the winglet by laying many plies at an angle. More in particular, many plies at zero degrees are positioned close to the upper surface, while closer to the bottom, there is an abundance of plies at -45 and 30 degrees. Moreover, the compliance matrix referred to the winglet, gives the information that the bending along the X and Y axis is opposite, meaning that when the wing flexes along the span of the wing, an opposite bending is induced in the cord direction. Practically this means that as the wing flexes with its extremity upwards, its camber increases, creating an airfoil section which produces increased lift. The complete winglet stacking sequence, presented in the following table, is made up of 34 plies which create a 31.84 mm thick asymmetric laminate.

Ply n°	1	2	3-4	5-6	7-8	9-13	14-15	16	17-18	19
g/mm^2	500	500	1500	1500	1500	1500	1500	500	1500	1500
orientation	45	-45	0	-45	45	0	-45	-45	90	-30

Ply n°	20-21	22-25	26-27	28	29-30	31-32	33	34
g/mm^2	1500	1500	1500	1500	1500	1500	500	500
orientation	45	0	-30	45	-30	0	-45	45

Table 17: Winglet complete stacking sequence

The lay-up process on the central foil and winglets must be done in parallel, allowing to use continuous cloths when possible. In particular, the plies which are continued across the two elements, are plies number from 1 to 5 and from 15 to 30.

On the contrary, the bending moment calculated on the elevator is significantly lower compared to the main foil. Rigidity on the elevator is crucial to maintain the correct vessel setup and control during any condition, hence the same stacking sequence used on the central foil is used. All the considerations mentioned for the central foil are also valid. The use of the same stacking sequence is an additional small design feature which reduces the chance of the boat builders to make any errors.

11.4.2 Struts & Rudder

All vertical elements are loaded in a similar way: the main loading condition is compression, added with bending induced by the strut vertical angle and the drift or rudder angles during turns.

To resist buckling, the structure must be rigid in all directions, hence a symmetric and balanced stacking sequence must be chosen. Symmetric ply properties introduced earlier are

still valid also for this particular stacking sequence, while a balanced stacking is achieved when the same number of plies placed at an angle, are balanced by the same amount placed at the opposite angle. The effect of such stacking sequence is that in plane forces and shear deformations are uncoupled. Additionally, the bending moment can be addressed by placing the outer plies along the span length.

A stacking sequence that fits these requisites is the same that was used on the central foil, and is presented in Table 16.

11.4.3 Connections

The most stressed part of the structure are the joints between the vertical elements and the horizontal ones, this is why these areas must be reinforced. In addition to this, the different elements must be joined permanently, and this is done with the combined action of structural adhesive, metallic bolts and further lamination to create a smooth transition between the parts.

Regarding the case of the main foil, the connection areas are described by bulbs that will have the double task of hosting the electric motors, but also serving as a structural connection between the three elements at play: the winglet, the central foil and the strut. The bulb is bolted to the vertical struts and must have a hinged opening on the bottom surface to allow the motor installation and maintenance, but at the same time it must be water tight. Internally the bulb must also host the supports for the engine bed, and engine shaft. Due to the complexity of the part, the structural sizing of this element should be assessed in detail, hence the lamination plan for this element is skipped since it goes out of the scope of this work.

During lamination, a thick steel threaded plate is inserted inside the carbon laminate on the vertical elements (struts and rudder). This is done to reinforce the area, and so that two bolts can be threaded onto the plate. Direct contact between the metal and the fiber must be avoided to prevent galvanic corrosion, this could be done for example with a polymeric coating or with an additional ply of glass fiber. The plate and bolts are sized according to Eurocode, a set of European standards that provide a common approach for engineering structures. The sizing procedure consists in calculating the shear load acting on each bolt, and dividing the result by the bolt's material shear strength. In turn, this result is compared with standard bolt sizes and a suitable bolt is selected. At the same time the plate is also sized: the bearing stress is calculated as the shear load, divided by the bolt diameter and the plate thickness. Since the shear load must be smaller than the yield strength, the only incognita (minimum plate thickness) is obtained. The bolt length is calculated taking into account the wing composite thickness, the steel plate thickness and the nut and washer sizes. The expected plate thickness is 6 mm on the main foil and 2 mm on the elevator, paired with a bolt diameter of 10 mm and 8 mm respectively.

The assembly process consists in firstly preparing the horizontal main foil by joining the two

wiglets together with the central foil and two bulbs. Then the struts are joined with the vertical struts by means the metallic bolts and the motors are fitted. All joints are reinforced with a structural adhesive compound, and additional E-glass fiber plies are laid to further stiffen the area. A total of 15 additional UD 100 g/m^2 are applied along the junction. To prevent the formation of any areas rich in resin, a small tongue of foam previously machined is applied to improve the performance of the connection. Potential resin bags can lead to cracks and stress concentration zones, resulting in weak spots.

11.5 FEA analysis

To validate the findings obtained with the CLT, a higher accuracy simulation is performed using the Solidworks software. The results from the analytical study serve as a starting point for more detailed FEA modelling of the problem. A total of four different cases are analysed: the main foil and rudder systems for a static straight course, and as was presented earlier, a steering condition where a drift angle of 5 degrees, and a rudder angle of 10 degrees are tested.

The 3D model is prepared for the analysis by acknowledging that Solidworks models the surfaces as shells. Consequently, the hydrofoil is modelled as two shells for the horizontal elements and one single enveloping shell on the vertical elements. Each shell is assigned its own orientation, offset and specific stacking sequence. To ensure the boundary condition is applied appropriately, the vertical elements are extended in height and the connection between them and the horizontal elements are modeled as a rigid bounded connection without any bulb for simplicity. Finally, the external loads are applied, and the mesh is prepared, as shown hereafter.

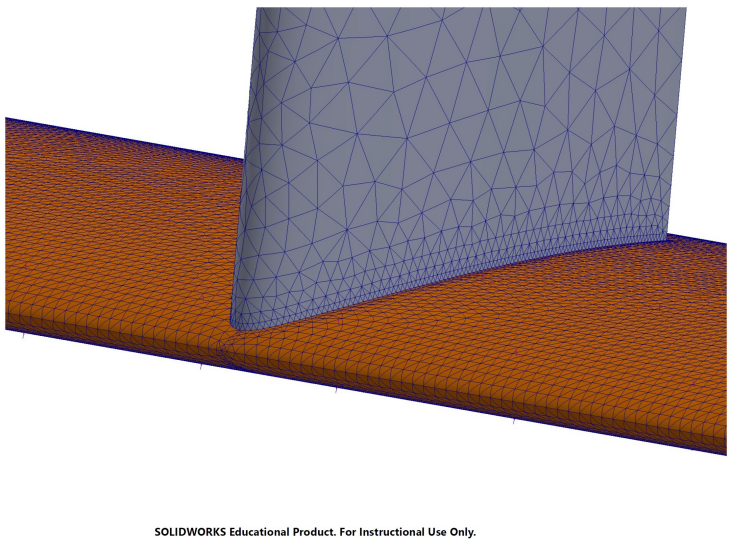

Figure 20: Rudder mesh detail

Triangular mesh cells are used, with 104k nodes on the main foil and 61k on the rudder T-foil. These nodes are distributed across their entire surfaces, with particular attention to the connections between components and areas where the highest stresses occur. Here the minimum element size is respectively equal to 2.46 mm and 1.89 mm on the main foil and rudder. A smaller mesh size is used on the surface of horizontal foils compared to the vertical ones, and in turn, more detail is given to the areas with high curvature which are the areas where there are greater pressure gradients, hence larger forces (aka leading edge). This is done to enhance the algorithm performance in areas where the stresses and displacement variations are largest. Figure 20 shows the mesh rudder detail as an example, which is very similar to the main foil and struts connection mesh.

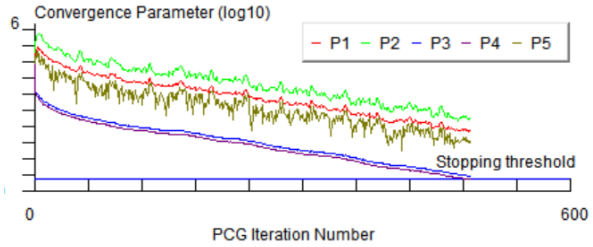

Figure 21: Convergence rate for the main foil simulation when turning

All simulations yield solutions that dovetail with the analytical calculations without any error messages. The solution is reached after a larger number of iterations if considering the more complex problem when both elevator and rudder blade produce lift. For the straight course scenario, the convergence rate is steep, and a solution is reached in fewer than 300 iterations. However, for large drift angles, the solution is achieved after approximately 500 iterations, as shown in Figure 21.

By examining the main foil deformation plot in Figure 22, it is evident that the winglets experience the most deformation, as expected. In the straight course scenario, the outermost winglet section rotates by -5.08 degrees, with a maximum displacement of 73.15 mm, mostly upwards in the Z direction, without considering the fluid structure interaction. Additional bending is expected on the winglets induced by the twisted winglet. The maximum bending on the central foil is 8.27 mm, which is 11% of the total winglet displacement. The maximum displacement on the vertical struts is located in the lower most extremity, where they connect to the horizontal main foil. In the straight course scenario, this point translates 1.5 mm inwards towards the centerline because of the bending on the central foil. The displacement of the same point increases to 49.4 mm when the maximum lateral drift angle is included in the study (when the vessel is turning). However, it is important to note that the external loads are increased by 3.5 times, hence such a displacement is unlikely to occur in reality.

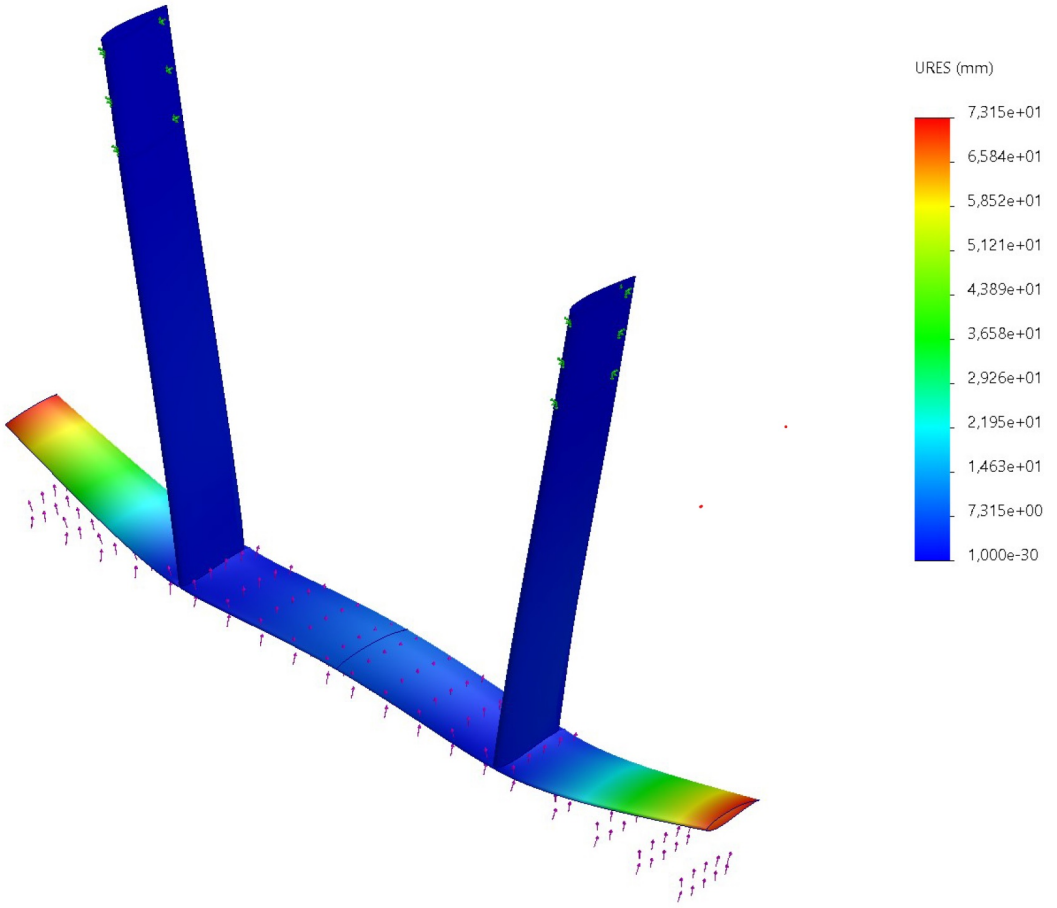

Figure 22: Main foil deformation plot during a straight line course

Figure 23 demonstrates how the lower extremity of the elevator is the one which has the largest movement, with a displacement of 1.59 mm. The cantilever section of the elevator is short and combined with the lower load compared to the main foil winglet, a more rigid wing is achieved. In this case no torsion is noted due to the fact that the rudder is centered with respect to the vertical strut, and the ply lay up doesn't allow torsion. Under static load, the rudder strut displacement is less than a tenth of a millimeter, but it increases to 151 mm when the rudder is placed at 10 degrees, as presented in the figure.

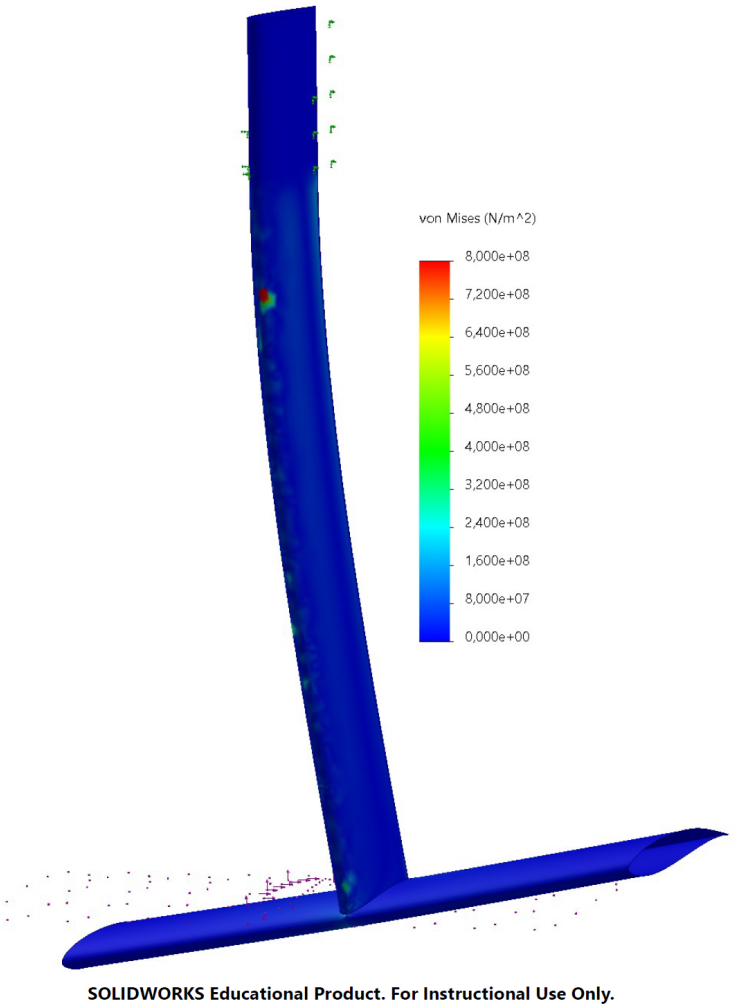

Figure 23: Rudder stress plot when placed at a 10 degree angle

Both the main foil and rudder assemblies pass the safety factor analysis with a factor of 3, indicating that the structure can withstand the imposed loads. The external loads used in the simulations were multiplied by a factor of 3.5, and anyways the structure fulfills the safety requirements, meaning that the structure could have the potential of being lightened to reduce weight, cost and manufacturing time. However, the struts, the central foil, rudder and elevator are all elements which are structurally driven by the deformation which is needed to be small. This suggests that the material is exploited to give rigidity and is far from its strength limits, as shown in Figure 23. Here a singularity is evident on the leading edge of the rudder, a mesh refinement should be made in this region to better assess the structural integrity of the vertical rudder, but this was limited by the mesh count imposed by the available Solidworks licence. The region which is not driven by displacement but instead is driven by strength are the two winglets, which must deform as much as possible without

breaking. Being these elements very thick, interlaminar shear stress must also be considered to prevent delamination. The material's shear stress threshold is set at 343 MPa, and the maximum shear stress measured near the root of the winglet is 100 times smaller than the threshold. This result is expected due to the maximum bending moment and curvature in this area, making it the first to potentially delaminate, although the results of the analysis prove that this will not occur.

The difference in results between the analytical and FEA analyses highlights the simplifications made using the two methods. These results are not thoroughly compared due to the large number of different assumptions adopted, making the comparison irrelevant. It must be noted, however, that the software also makes some simplifications by creating shells starting from the geometry surfaces. A more truthful representation of reality would be achieved by using solids instead of shells, but this option is not available in Solidworks. Additionally, a detailed fatigue analysis is recommended, especially for the winglets, which are the elements designed to flex the most, as well as considering the interaction between the two actors at play: the fluid which generates the loads and the structure.

12 Limitations and indications for future research

This contribution is an initial analysis of a variety of aspects related to the design of the 9-meter model of the foiling trimaran ferry. Due to the limited scope of this thesis, it has not been possible to engage in a more detailed and systematic analysis of each sub-aspect and thus of the overall project. Future research, along with additional resources, and effective teamwork, will surely allow to greatly expand the scope of this project and its associated research results.

To begin with, the static forces and moments prediction spreadsheet could be replaced by a more detailed simulator capable of accounting for the vessel's dynamic behaviour during navigation. Notably, the initialization of Gomboc was part of the work carried out during the thesis time frame. Gomboc integrates a Velocity Prediction Program, real-time simulation, and an appendage design package (Wilkins, 2017) which began to be developed in 2010 by a team of people behind the new AC75's for the 37th America's Cup (Barcelona 2024). This tool allows the design of various appendages and performance assessments under different sailing conditions for both sailboats and powerboats. By incorporating detailed hydrodynamic and structural features (such as twist, airfoil shapes, transverse and longitudinal shapes, flexural and torsional properties, and shear centre coordinates), it is possible to rapidly test different foil designs, understand their performance, and conduct an optimization process. Once the desired configuration is identified, a 3D CAD model can be exported and imported into more refined CFD or FEA solvers for further refinement.

A significant challenge encountered during the *Gomboc* simulation of the trimaran ferry was the lack of a developed flight control system, which is crucial for the definitive stability assessment. Once stability is guaranteed, a further iteration of the airfoil selection process must be undertaken to enhance efficiency, following the same steps as the ones shown in Chapter 9. Approximated methods, like those presented in this work, can cause significant variations in the equilibrium configuration compared to real-world scenarios, leading to the optimization of shapes which work in reality at a different angle of attack. Therefore, a better approximation using a RANS-based solver, which provides a higher fidelity representation of lift coefficients, is necessary to achieve the better equilibrium position.

Upon obtaining the definitive foil shapes, a deeper refinement of hydrodynamic performance is essential. A systematic approach to reducing induced drag can be performed by creating a parametric CAD design of the foil, controlled by an optimization solver such as ModeFrontier. This solver couples the foil geometry with CFD simulation results to autonomously find the best performing shape. Achieving this requires developing a script to systematically create successful meshes and for the post process of results, as well as a highly developed computing unit.

Once the best performing shape is identified, a structural assessment with a higher level of accuracy than this work can be conducted, adopting 3D shapes instead of two-dimensional shells, sizing the bulbs, and assessing fluid-structure interaction. As previously mentioned, further research is required into the choice of motor and propeller and into designing a flight control system.

13 Conclusions

In this thesis, a new hydrofoiling vessel concept was developed to combine the benefits of forerunner surface-piercing foils with modern submerged flap-oriented solutions. The result is a ferry capable of transporting up to 40 passengers with low carbon emissions. The examined solution involves a fixed, fully submerged wing that lifts the vessel from the water, significantly reducing drag and ensuring a cost-effective solution with no submerged mechanical elements, that could lead to costly maintenance or service disruptions. The design of the 9-meter model vessel was addressed to ensure the viability of the full-size solution.

Initially, a spreadsheet based on *Prandtl's lifting line theory* was created to predict the forces and moments produced by the hydrofoil. This simplified tool allowed for quick and effective assessments of various foil geometries without needing 3D modelling, meshes, or computationally expensive simulations. To validate the tool, CFD simulations were performed, assigning reduction factors to each foil section in the spreadsheet to better represent reality. This tool was crucial in finding the equilibrium attitude of the vessel for the three studied

conditions: lift-off, cruise, and maximum speed. Once equilibrium was achieved, the tool was used to assess static stability and ensure the foiling system was stable. Various designs were tested to identify the best-performing configuration, ensuring safety and comfort. To prevent rolling issues, solutions like tip ventilation and additional foil stabilizers were explored, each with their benefits and disadvantages. The airfoil selection process was also conducted to allocate the most suitable shape to each hydrofoil section, avoiding cavitation by selecting a cambered airfoil for the main foil and flatter shapes for the elevator. Symmetrical shapes were instead chosen for the vertical elements, with a more slender shape for the main struts and a thicker one on the rudder. Given the chosen 'optimized' configuration presented in Table 3, the main foil and elevator must be respectively installed at a positive 4.3 and 2.6 degree angle, these figures were obtained to achieve a level flight at cruise speed. This arrangement results in a positive pitch attitude of the whole vessel during lift-off equal to 4.6 degrees with the elevator being titled at a negative 0.5 degrees, while the effect is opposite at maximum speed where the attitude of the vessel becomes -2.9 degrees and the elevator attitude equal to positive 1 degree.

The designed wings were further refined to reduce induced drag using Ansys CFX. Although a more systematic approach would have been more effective, a simplified methodology was preferred, involving testing ranges of the same design feature and then integrating the best feature into the final design. The main foil, described by an elliptical planform shape with its extremity translated aft by 50 mm, paired with a small tip shape and a bulb with a thick head and thin tail, increased the wing's performance by 51%. The elliptical elevator, connected to the rudder blade via a slim bulb, achieved a 24% increase in performance.

Finally, the design was assessed for structural integrity. The bending moments acting on the structure were computed using analytical solid mechanics theory, revealing that the most stressed areas are the joints between vertical and horizontal elements. To determine the appropriate stacking sequence for each element, the results were used both for the initial airfoil selection and as input parameters in classical lamination theory. The chosen laminates were validated in Solidworks via an FEA analysis, and all passed the structural test, although further optimization with a more detailed tool could enhance results.

Gomboc was partially used to simulate the concept's behavior in different sea states and loading conditions. However, as previously mentioned, the lack of a flight control system impeded the complete outcome of this analysis. Implementing this system is crucial for a comprehensive validation of the project. Although not covered within the scope of this work, the foiling trimaran showed promising results that suggest the potential for a successful design. Nevertheless, this design is limiting in the fact that when turning, very sharp corners cannot be reached. Instead, sailing should be optimized for predetermined routes with specific speed requirements, making this design more suitable for ferries or commercial vessels, ideally operating in calm seas, rivers, or lakes. It is not recommended for pleasure crafts, which are intended for versatile use in varying conditions.

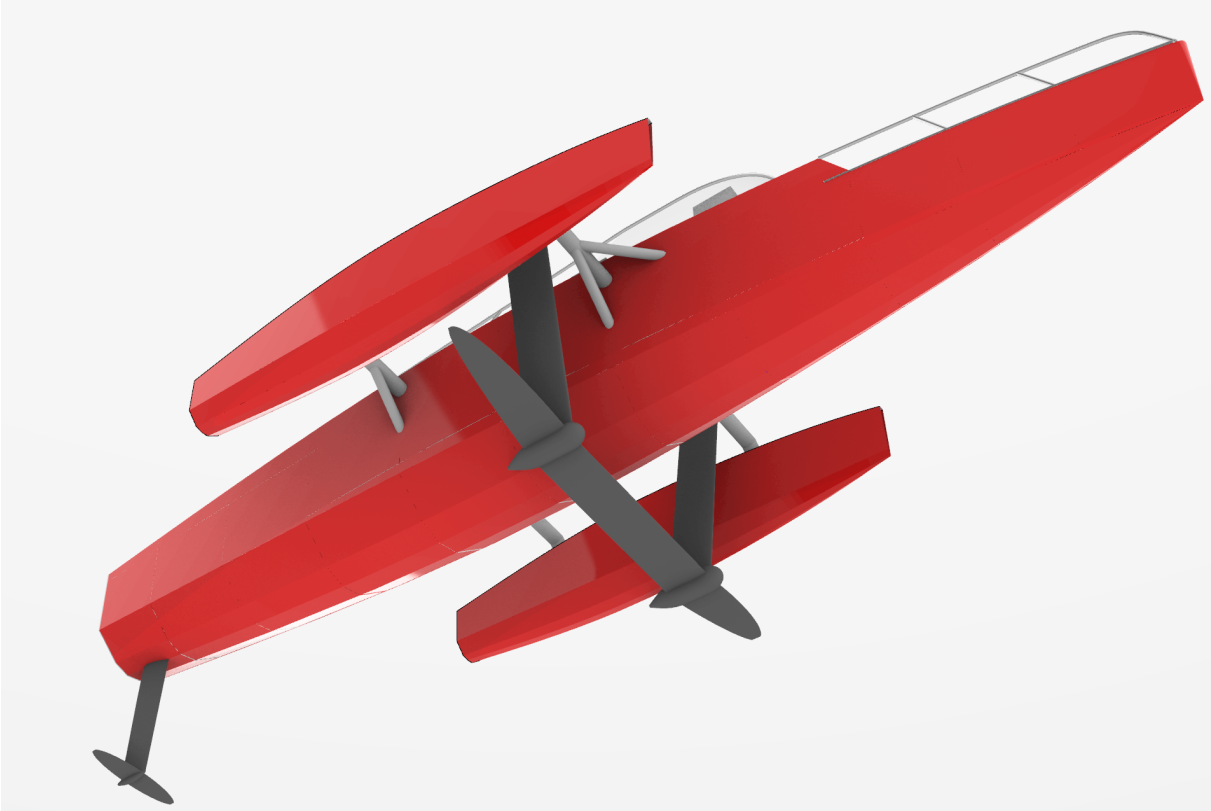

Figure 24: Final foil design mounted on the trimaran model

14 References

Gournay, L. (2022). Master thesis: The Hull Optimisation for an Open 60 IMOCA Single Handed Race yacht.

Fetting, C. (2020). The European green deal. ESDN Report, December, 2(9).

Acosta, A. J. (1973). Hydrofoils and hydrofoil craft. Annual Review of Fluid Mechanics, 5(1), 161-184.

McConaghy Boats, Emirates Team New Zeland (2022).
Chase Zero. URL: https://mcconaghyboats.com/yachts/chase-zero/

The Royal New Zealand Yacht Squadron Incorporated, Royal Yacht Squadron Limited (2021).
THE PROTOCOL GOVERNING THE 37TH AMERICA'S CUP. URL:
https://drive.google.com/file/d/1p1N0KDOIh9PtsJ5PLJT3UBCLUY1P1qeR/view

Candela (2024). P-12 Shuttle. URL: https://candela.com/p-12-shuttle/

Artemis Technologies (2022). E F-24 PASSENGER. URL:
https://www.artemistechnologies.co.uk/ef-24-passenger-ferry/

Miles, J. C., Johnson, B., Womack, J., & Franzen, I. (2007, March). SNAME's Stability Letter Improvement Project (SLIP) for Passenger Sailing Vessels. In SNAME Chesapeake Sailing Yacht Symposium (p. D021S002R005). SNAME.

International Organization for Standardization. (2009). ISO 22119: Intelligent transport systems — Full speed range adaptive cruise control (FSRA) systems — Performance requirements and test procedures. ISO/TC 204, Intelligent transport systems.

National Coastal Monitoring, (2023) Chichester Harbour buoy wave monitoring. URL: https://coastalmonito

Hella, A. H. (2021). Modeling and Control of a Foiling Trimaran Sailboat (Master's thesis, NTNU).

Eggert, F. (2018). Flight dynamics and stability of a hydrofoiling international moth with a dynamic velocity prediction program (dvpp). en. MA thesis. Berlin, Germany: TU Berlin.

Meyer, J. R. Hydrofoil overview-a brief tutorial. The International Hydrofoil Society, 1.

Bai, J., & Kim, Y. (2010). Control of the vertical motion of a hydrofoil vessel. Ships and Offshore Structures, 5(3), 189-198.

Li, L., Qiao, L., Xu, J., & Bai, J. (2023). Effects of Static Stability Margin on Aerodynamic Design Optimization of Truss-Braced Wing Aircraft. Aerospace, 10(7), 603.

Norton, F. H. (1924). A study of longitudinal dynamic stability in flight (No. NACA-TR-170).

Acosta, A. J. (1973). Hydrofoils and hydrofoil craft. Annual Review of Fluid Mechanics, 5(1), 161-184.

Sadraey, M. H. (2012). Aircraft design: A systems engineering approach. John Wiley & Sons.

Münch, C., Ausoni, P., Braun, O., Farhat, M., & Avellan, F. (2010). Fluid–structure coupling for an oscillating hydrofoil. Journal of Fluids and Structures, 26(6), 1018-1033.

Hammami, A., Gebart, B. R. (2000). Analysis of the vacuum infusion molding process. Polymer composites, 21(1), 28-40.

Skripkin, S. G., Tsoy, M. A., & Kravtsova, A. Y. (2022). Experimental study of cavitating flow around a NACA 0012 hydrofoil in a slit channel. Scientific Reports, 12(1), 11182.

Khan, S. A., Bashir, M., Baig, M. A. A., Ali, F. A. G. M. (2020). Comparing the effect of different turbulence models on the CFD predictions of NACA0018 airfoil aerodynamics. CFD Letters, 12(3), 1-10.

GongZhang, H., & Axtelius, E. (2020). Aircraft winglet design.

Ning, S. A., & Kroo, I. (2010). Multidisciplinary considerations in the design of wings and wing tip devices. Journal of aircraft, 47(2), 534-543.

Kim, U. (2015). Numerical analysis and optimization of wing-tip designs. San Jose State University.

Rajendran, S. (2012). Design of Parametric Winglets and Wing tip devices: A conceptual design approach.

Godø, J. M. K., Steen, S., & Faltinsen, O. M. (2024). A resistance model for hydrofoil fast ferries with fully submerged foil systems. Ocean Engineering, 301, 117503.

Brito M, 2019. Use of Gomboc to Predict the Performance of a Hydro-Foiled Moth. Internship report. The University of Auckland.

Wilkins, I. (2017). Gomboc: A design high-flier for ETNZ. BREEZE, 34–37.

Appendices

A Weight Estimate

	Tot. Weight (kg)	Tot. Weight (kg) inc. margin	LCG (m)	VCG (m)	TCG (m)	Ixx (Kg*m^2)	Iyy (Kg*m^2)	Izz (Kg*m^2)
Structure	400,18	497,88	4,22	0,68	0,00	232,68	8087,76	7855,08
Propulsion	198,00	217,80	5,10	-1,28	0,00	324,40	5474,38	5149,98
Electrical Sys.	613,43	649,05	4,07	0,73	0,00	329,43	10841,51	10512,08
Nav & Comms	11,80	12,39	4,62	1,07	2,54	103,92	275,17	351,25
Auxiliary Sys.	391,24	428,45	3,19	-0,04	0,00	152,32	6433,63	6281,31
Outfit	53,50	56,18	4,16	0,60	0,00	21,66	978,12	956,46
Total lightship	1668,15	1861,75	4,03	0,30	0,02	1164,41	32090,57	31106,16

Table 18: Appendix: Weight estimate

B Forces and Moments

B.1 Input variables

- Position of centre of mass (CG) relative to (0,0,0) (m)
- Position of Centre of Rotation relative to (0,0,0). (m)
- Boat speed (knots)
- Port engine power (installed) (Kw)
- Stbd. engine power (installed) (Kw)
- Engine loss (Efficiency coefficient ranges from zero to one as the delivered power is less than 100% and also at lower speeds, not all of the available power is required. This is automatically adjusted within a loop of the program so as to match the effective power required at a specific speed, and resistance depending upon the varying configuration. Hence the program generates this efficiency coefficient)
- Mass of the boat (kg)
- Mass moment of inertia (Ixx, Iyy, Izz) (kgm2)
- Trajectory/ turning circle radius (m)

- Ride height at CL (WL to USK) (m)
- Total Main strut height (Distance from USK to actual foil) (metres)
- Chord of Strut (Main Masts) (m)
- Distance between struts. (m)
- Span of Horizontal Main Foil (m)
- Chord of Horizontal Main Foil (m)
- Initial main foil angle of attack (degrees)
- Bulb length (only for thrust force position, the bulb drag is not calculated) (m)
- Span of tips (m)
- Chord of Tips (m)
- Angle of starboard tip to the horizontal Plane (degrees)
- (Note the port tip is the same angle as starboard, but negatively signed)
- Initial tip angle of attack (degrees)
- (this is currently set as the same as the main foil)
- Total Rudder Blade/strut height (m) (Distance from USK to rudder foil)
- Span of Horizontal Rudder Foil (m)
- Rudder Blade Rudder Foil (Elevator) Chord (m)
- Initial horizontal rudder foil angle of attack (degrees)
- X distance between LE of main foil and LE of rudder (m)
- Z distance difference in height between main and rudder horizontal foils. If rudder foil is lower, then distance Z is positive. If the rudder foil is higher, then this distance is recorded as negative.
- Airfoil NACA section for every element of the system.

B.2 Spreadsheet screenshot

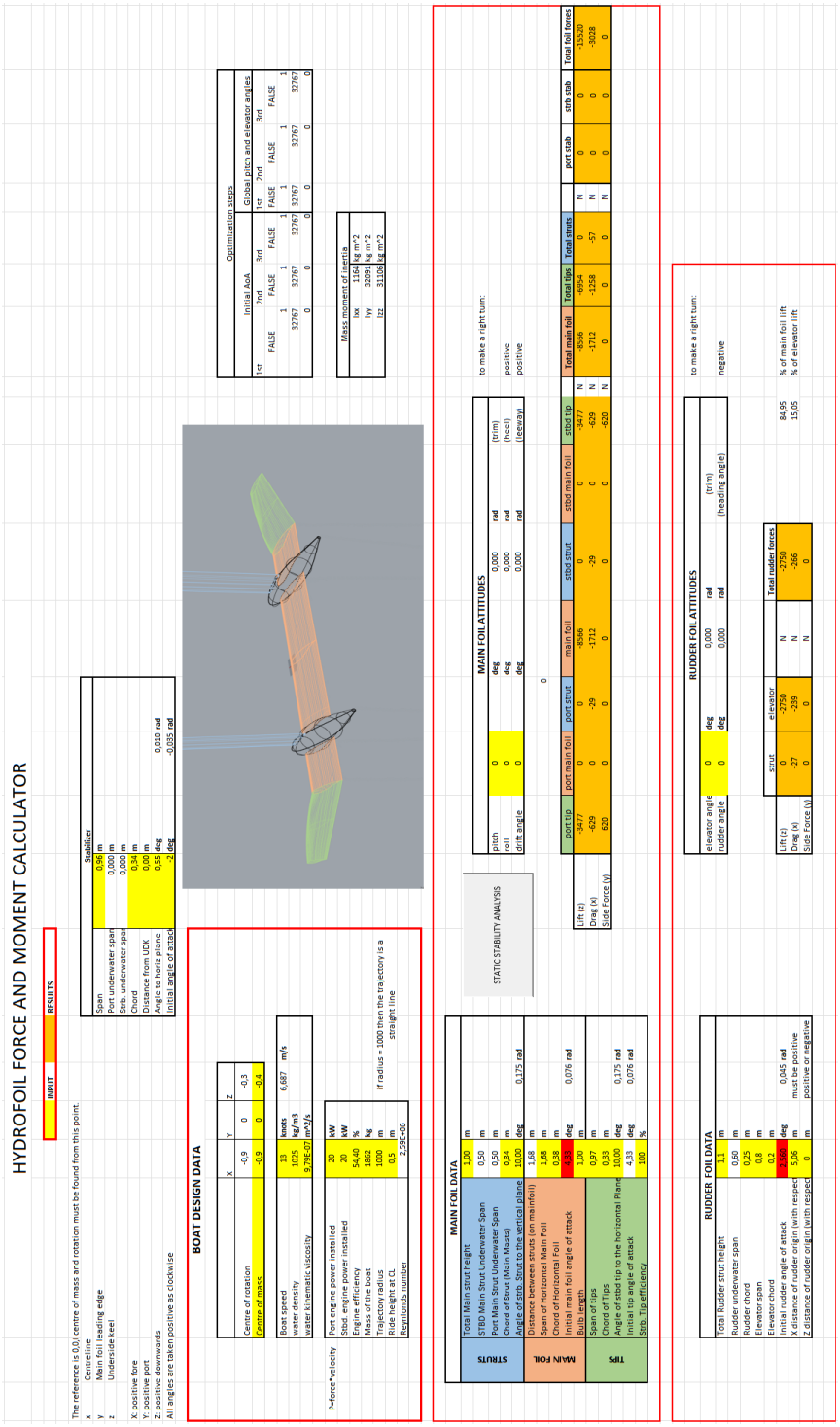

Figure 25: Appendix: Extract of "Forces and Moments" spreadsheet

C Analysis of different designs

						WINGLET ANGLE							MAINFOIL SPAN	
				Base design	Winglet angle= -30	Winglet angle= -20	Winglet angle= -10	Winglet angle= 0	Winglet angle= 10	Winglet angle= 20	Winglet angle= 30	Total span main: 3,3	Total span main: 3,6
			Main AoA	2,02342322	2,37811	2,14138	2,00963	1,9533	1,97943	2,10664	2,31231	2,14715	2,1444
			Rudd AoA	-2,00895671	-2,0716	-2,05707	-2,04121	-2,028	-2,0161	-2,0004	-1,9861	-1,9764	-1,9561
			Throttle	56,2449726	59,9561	57,4706	55,9577	55,406	55,7689	57,1761	59,5093	49,4862	45,9694
ATTITUDE OF THE VESSEL	2 degree change in roll		Mx	25	-48	-33	-17	1	18	35	49	31	36
			My	-41	-45	-42	-40	-40	-40	-42	-44	-36	-35
			Mz	3	6	5	5	4	4	3	2	4	5
	2 degree change in pitch		Mx	1	0	0	0	0	0	0	0	0	0
			My	-12898	-13355	-13113	-12959	-12872	-12872	-12954	-13108	-12831	-12744
			Mz	-1	0	0	0	0	0	0	0	0	0
	2 degree change in yaw		Mx	-5603	-6457	-6309	-6034	-5780	-5632	-5601	-5662	-5575	-5537
			My	-633	-783	-690	-647	-639	-633	-660	-755	-642	-640
			Mz	-6958	-6658	-6766	-6890	-6968	-6974	-6924	-6882	-6859	-6806
ATTITUDE OF THE RUDDER RELATIVE TO THE	2 degree change in elevator		Mx	1	0	0	0	0	0	0	0	0	0
			My	-14447	-14465	-14461	-14456	-14452	-14449	-14444	-14442	-14440	-14437
			Mz	-1	0	0	0	0	0	0	0	0	0
	2 degree change in rudder		Mx	-3653	-3653	-3653	-3653	-3653	-3653	-3653	-3653	-3653	-3652
			My	-437	-437	-437	-437	-437	-437	-436	-436	-436	-436
			Mz	-8567	-8569	-8568	-8568	-8568	-8567	-8567	-8566	-8566	-8566
					Winglet angle= -30	Winglet angle= -20	Winglet angle= -10	Winglet angle= 0	Winglet angle= 10	Winglet angle= 20	Winglet angle= 30	Total span main: 3,3	Total span main: 3,6
			Throttle	56,2449726	-7%	-2%	1%	1%	1%	-2%	-6%	12%	18%
ATTITUDE OF THE VESSEL	X	2 degree change in roll	Mx	25	292%	232%	168%	96%	28%	-40%	-96%	-24%	-44%
	Y		My	-41	-11%	-3%	2%	2%	2%	-3%	-8%	11%	14%
	Z		Mz	3	-81%	-51%	-51%	-20%	-20%	10%	40%	-20%	-51%
	X	2 degree change in pitch	Mx										
	Y		My	-12898	4%	2%	0%	0%	0%	0%	2%	-1%	-1%
	Z		Mz	-1									
	X	2 degree change in yaw	Mx	-5603	-15%	-13%	-8%	-3%	-1%	0%	-1%	1%	1%
	Y		My	-633	-24%	-9%	-2%	-1%	0%	-4%	-19%	-1%	-1%
	Z		Mz	-6958	-4%	-3%	-1%	0%	0%	0%	-1%	-1%	-2%
ATTITUDE OF THE RUDDER RELATIVE TO THE	X	2 degree change in elevator	Mx	1									
	Y		My	-14447	0%	0%	0%	0%	0%	0%	0%	0%	0%
	Z		Mz	-1									
	X	2 degree change in rudder	Mx	-3653	0%	0%	0%	0%	0%	0%	0%	0%	0%
	Y		My	-437	0%	0%	0%	0%	0%	0%	0%	0%	0%
	Z		Mz	-8567	0%	0%	0%	0%	0%	0%	0%	0%	0%

Figure 26: Appendix: Extract of "Data for analysis of different designs" spreadsheet

D Airfoil Selection

D.1 Tested shapes

D.1.1 Main foil

ID	Description	Thickness	T. location	Camber	C. location
1	Eppler 817	10,98	32,83	2,88	68,87
2	#1 with larger camber	11,04	32,83	3,37	71,17
3	#1 with lower camber	10,98	32,63	2,87	75,38
4	#1 with larger camber position	10,05	32,83	2,87	66,67
5	#1 with lower camber position	11,04	32,83	2,38	71,07
6	#1 with larger thickness	11,55	32,83	2,87	71,07
7	#1 with lower thickness	10,54	32,83	2,87	71,07
8	#1 with larger thickness position	10,05	37,64	2,87	68,87
9	#1 with lower thickness position	10,94	28,23	2,87	66,77
10	#1 mutant n1	10,57	32,93	2,99	63,66
11	#1 mutant n2	10,56	32,53	3,19	66,67
12	#1 mutant n3	10,76	32,53	3,49	68,87
13	#1 mutant n4	9,05	32,53	3,48	71,07
14	#1 mutant n5	10,44	28,23	2,38	66,67
15	#1 mutant n6	11,04	32,83	3,79	71,07
16	#1 mutant n7	11,87	32,83	4,59	71,07
17	#1 mutant n8	12,15	27,93	5,28	68,87
18	#1 mutant n9	11,04	32,83	6,88	78,78
19	#1 mutant n10	12,38	32,83	4,29	66,67
20	#1 mutant n11	10,98	52,35	6,88	71,07
21	#1 mutant n12	10,97	15,82	4,47	68,87
22	#1 mutant n13	11,05	32,93	5,19	57,26
23	#1 mutant n14	11,06	32,93	5,78	53,05
24	#1 mutant n15	11,05	32,83	3,79	62,06
25	#1 mutant n16	12,48	32,83	4,27	63,66
26	#1 mutant n17	12,39	32,93	4,28	47,65
27	#1 mutant n18	12,4	32,93	4,59	47,65
28	#1 mutant n19	12,38	32,93	4,28	52,35
29	#1 mutant n20	11,39	32,83	4,26	66,67
30	#1 mutant n21	12,41	28,03	4,25	63,66
31	#1 mutant n22	12,58	32,83	4,29	66,67
32	#1 mutant n23	12,68	32,83	4,49	66,67

Continued on next page

– continued from previous page

ID	Description	Thickness	T. location	Camber	C. location
33	Best performing #1 mutant	11,46	32,53	3,48	71,07
34	GA 30U-615	15	30,03	4,49	44,94
35	Hybrid: 30% #34 - 70% #33	12,53	31,03	3,44	60,66
36	Hybrid: 35% #34 - 65% #33	12,7	30,93	3,46	60,56
37	Hybrid: 36% #34 - 64% #33	12,74	30,93	3,47	60,56
38	Hybrid: 36,8% #34 - 63,2% #33	12,77	30,93	3,47	60,56
39	Hybrid: 37% #34 - 63% #33	12,77	30,93	3,47	60,46
40	Hybrid: 37,5% #34 - 62,5% #33	12,79	30,93	3,48	60,46
41	Hybrid: 40% #34 - 60% #33	12,88	30,93	3,49	60,46
42	Hybrid: 50% #34 - 50% #33	13,2	30,93	3,58	60,36
43	Hybrid: 60% #34 - 40% #33	13,59	30,83	3,66	60,15
44	Hybrid: 70% #34 - 30% #33	13,9	30,73	3,75	59,95
45	Hybrid: 80% #34 - 20% #33	14,29	30,63	3,83	59,85
46	Hybrid: 90% #34 - 10% #33	14,59	30,53	3,92	59,64
47	#34 with same X location	15	30,03	4,49	44,94
48	Hybrid: 40% #47 - 60% #33	12,89	31,03	3,48	60,56
49	Hybrid: 50% #47 - 50% #33	13,19	31,03	3,56	60,36
50	Hybrid: 60% #47 - 40% #33	13,6	30,93	3,67	60,15
51	Hybrid: 70% #47 - 30% #33	13,89	30,83	3,75	59,95
52	Hybrid: 80% #47 - 20% #33	14,29	30,63	3,83	59,85
53	Hybrid: 90% #47 - 10% #33	14,6	30,53	3,92	59,74
54	90% #47 with 5% added camber	14,6	30,53	4,2	59,74
55	90% #47 with 10% added camber	14,6	30,53	4,5	59,74
56	Hybrid: 40% #55 - 60% #33	10,88	31,33	3,38	63,16
57	Hybrid: 50% #55 - 50% #33	10,73	31,03	3,4	60,06
58	Hybrid: 60% #55 - 40% #33	10,59	31,03	3,45	55,86
59	Hybrid: 25% #52 - 75% #33	11,1	31,33	3,29	67,37
60	Hybrid: 40% #52 - 60% #33	10,88	31,23	3,21	63,26
61	Hybrid: 50% #52 - 50% #33	10,74	31,03	3,18	60,36
62	Hybrid: 51% #52 - 49% #33	10,72	31,03	3,18	60,26
63	Hybrid: 52% #52 - 48% #33	10,71	31,03	3,17	60,26
64	Hybrid: 53% #52 - 47% #33	10,69	31,03	3,17	60,26
65	Hybrid: 54% #52 - 46% #33	10,68	31,03	3,17	58,86
66	Hybrid: 55% #52 - 45% #33	10,66	31,03	3,17	58,86
67	Hybrid: 60% #52 - 40% #33	10,59	31,03	3,17	57,36
68	Hybrid: 75% #52 - 25% #33	10,37	29,93	3,23	5,05

Table 19: Appendix: Main foil tested shapes

D.1.2 Elevator

ID	Description	Thickness	T. location	Camber	C. location
1	EPPLER 908	9,00	44,35	2,77	66,27
2	#1 with much larger camber	9,00	44,35	4,03	66,27
3	#1 with larger camber	9,00	44,25	2,51	66,27
4	#1 with lower camber	9,00	44,25	3,02	66,27
5	#1 with larger camber position	9,00	44,25	2,78	70,27
6	#1 with lower camber position	9,00	44,25	2,78	61,06
7	#1 with larger thickness	10,00	44,25	2,79	66,27
8	#1 with lower thickness	8,00	44,25	2,79	66,27
9	#1 with largest thickness position	9,00	66,87	2,79	66,27
10	#1 with much larger thickness pos	9,00	58,76	2,79	66,27
11	#1 with larger thickness position	9,00	50,15	2,79	66,27
12	#1 with lower thickness position	9,00	39,44	2,79	66,27
13	#1 with camber:3.80 - Thick: 8.00	8,00	44,35	3,83	66,27
14	#1 with camber:3.80 - Thick: 8.20	8,20	44,35	3,83	66,27
15	#1 with camber:3.80 - Thick: 8.22	8,22	44,35	3,83	66,27
16	#1 with camber:3.80 - Thick: 8.24	8,24	44,35	3,83	66,27
17	#1 with camber:3.80 - Thick: 8.26	8,26	44,35	3,83	66,27
18	#1 with camber:3.80 - Thick: 8.28	8,28	44,35	3,83	66,27
19	#1 with camber:3.80 - Thick: 8.30	8,30	44,35	3,83	66,27
20	#1 with camber:3.80 - Thick: 8.36	8,36	44,35	3,83	66,27
21	#1 with camber:3.80 - Thick: 8.38	8,38	44,35	3,83	66,27
22	#1 with camber:3.80 - Thick: 8.40	8,40	44,35	3,83	66,27
23	#1 with camber:3.80 - Thick: 8.50	8,50	44,35	3,83	66,27
24	#1 with camber:3.80 - Thick: 8.50	9,00	44,35	3,83	50,25
25	#1 with camber:4.00 - Thick: 8.50	9,00	39,44	4,03	66,27
26	Hybrid: 40% #14 - 60% #5	8,68	44,25	3,2	68,77
27	Hybrid: 50% #14 - 50% #5	8,27	53,05	3,31	66,47
28	Hybrid: 60% #14 - 40% #6	8,52	44,25	3,4	67,37
29	A18	7,34	29,93	5,04	44,94
30	AG 24	8,41	26,03	2,22	45,45
31	AG 36	8,18	27,83	4,09	26,63
32	EH 1,0/9,0	8,99	28,73	1	25,93
33	Jukovsky f=0% t=9%	9,00	25,53	0	0
34	MH 62 9,3%	9,29	27,93	1,64	37,14
35	Prandtl-D	12,03	30,98	4,09	40,38
36	RoncZ	12,05	42,74	2,81	39,14

Continued on next page

– continued from previous page

ID	Description	Thickness	T. location	Camber	C. location
37	Hybrid: 40% #6 - 60% #13	8,40	44,35	3,4	64,57
38	Hybrid: 50% #6 - 50% #13	8,50	44,25	3,3	63,66
39	Hybrid: 60% #6 - 40% #13	8,60	44,35	3,2	63,76
40	Hybrid: 20% #33 - 80% #1	8,81	38,34	2,21	67,57
41	Hybrid: 25% #33 - 75% #1	8,78	38,24	2,07	67,57
42	Hybrid: 29% #33 - 71% #1	8,87	38,24	1,96	67,57
43	Hybrid: 20% #33 - 80% #1	8,75	38,14	1,94	67,57
44	Hybrid: 38% #33 - 62% #1	8,73	35,04	1,71	67,47
45	Hybrid: 42% #33 - 58% #1	8,73	34,94	1,66	67,47
46	Hybrid: 40% #33 - 60% #1	8,72	34,94	1,6	67,47
47	Hybrid: 50% #33 - 50% #1	8,72	31,83	1,38	67,47
48	Hybrid: 60% #33 - 40% #1	8,74	31,73	1,11	67,47
49	Hybrid: 30% #33 - 70% #1	8,78	28,63	0,83	67,47
50	Hybrid: 20% #33 - 80% #1	8,84	28,53	0,55	67,37
51	PW51	8,90	27,53	1,42	27,53
52	#51 with increased camber	8,90	27,53	2,04	27,53
53	Hybrid: 20% #30 - 80% #1	11,29	30,99	3,72	42,19
54	Hybrid: 30% #30 - 70% #1	10,92	30,99	3,53	42,29
55	Hybrid: 40% #30 - 60% #1	8,55	35,94	2,45	56,86
56	Hybrid: 50% #30 - 50% #1	8,49	34,44	2,4	55,36
57	Hybrid: 60% #30 - 40% #1	8,44	32,93	2,35	52,55
58	Hybrid: 60% #3 - 40% #35	10,22	41,94	2,77	50,05
59	Hybrid: 70% #3 - 30% #35	9,81	39,12	3,18	50,03
60	Hybrid: 60% #3 - 40% #36	10,10	36,41	3,29	49,92
61	Hybrid: 40% #51 - 60% #1	8,76	37,14	1,98	47,15
62	Hybrid: 50% #51 - 50% #1	8,74	34,94	1,84	47,05
63	Hybrid: 40% #61 - 60% #1	8,63	32,33	1,88	47,05
64	Hybrid: 50% #61 - 50% #1	8,66	32,23	1,76	41,94
65	Hybrid: 60% #61 - 40% #1	8,69	31,13	1,66	37,04
66	#63 with increased camber n1	8,63	32,33	2,31	46,95
67	#63 with increased camber n2	8,63	32,33	2,51	46,95

Table 20: Appendix: Elevator tested shapes

D.1.3 Struts

ID	Description	Thickness	T. location
1	Eppler 473	16,19	21,22
2	Eppler 479	16,57	25,73
3	Eppler E837	16,11	36,94
4	Eppler E838	18,37	37,24
5	FX 71-L-150/20 AIRFOIL	15,00	33,93
6	FX 71-L-150/25 AIRFOIL	15,00	33,93
7	FX 71-L-150/30 AIRFOIL	15,00	33,93
8	Joukovsky f=0% t=15%	14,99	24,62
9	LWK 80-150/K25	14,05	40,24
10	NACA 0018	18,00	30,03
11	NACA 16-015	15,00	49,95
12	NACA 16-018	18,00	49,95
13	NACA 63(3)-018	18,01	33,93
14	NACA 642-015 AIRFOIL	14,96	35,04
15	NACA 642-015A AIRFOIL	14,97	39,94
16	NACA 66-018	17,99	45,05
17	S1014	16,51	42,24
18	S1016	14,48	41,84
19	US1000ROOT	18,57	27,13
20	WORTMANN FX L V-152 AIRFOIL	15,28	34,03

Table 21: Appendix: Struts tested shapes

D.2 Strut performance ranking

Efficiency		Lift		Drag		Moment	
weight = 0,3		weight = 0,3		weight = 0,2		weight = 0,2	
ID #	Points	ID #	Points	ID #	Points	ID #	Points
18	6	**12**	6	**9**	4	**12**	4
9	5,7	**11**	5,7	**18**	3,8	**11**	3,8
17	5,4	**9**	5,4	**17**	3,6	**19**	3,6
16	5,1	**19**	5,1	**16**	3,4	**9**	3,4
3	4,8	**7**	4,8	**3**	3,2	**1**	3,2
15	4,5	**10**	4,5	**15**	3	**10**	3
14	4,2	**6**	4,2	**4**	2,8	**7**	2,8
4	3,9	**15**	3,9	**14**	2,6	**6**	2,6
13	3,6	**1**	3,6	**13**	2,4	**2**	2,4
8	3,3	**5**	3,3	**8**	2,2	**5**	2,2
2	3	**2**	3	**2**	2	**8**	2
10	2,7	**3**	2,7	**10**	1,8	**15**	1,8
19	2,4	**14**	2,4	**19**	1,6	**3**	1,6
1	2,1	**8**	2,1	**1**	1,4	**14**	1,4
7	1,8	**4**	1,8	**7**	1,2	**13**	1,2
6	1,5	**16**	1,5	**20**	1	**17**	1
5	1,2	**17**	1,2	**6**	0,8	**18**	0,8
11	0,9	**13**	0,9	**5**	0,6	**16**	0,6
12	0,6	**18**	0,6	**11**	0,4	**4**	0,4
20	0,3	**20**	0,3	**12**	0,2	**20**	0,2

ID #	TOT. SCORE
#1	10,3
#2	10,4
#3	12,3
#4	8,9
#5	7,3
#6	9,1
#7	10,6
#8	9,6
#9	18,5
#10	12
#11	10,8
#12	10,8
#13	8,1
#14	10,6
#15	13,2
#16	10,6
#17	11,2
#18	11,2
#19	12,7
#20	1,8

Table 22: Appendix: Strut performance ranking

E Material properties

Resin	Young's M. (MPa)	Shear M. (MPa)	Poisson's Ratio	Density (g/cm^6)	Tensile S. (MPa)	Compressive S. (MPa)	Shear S. (MPa)
ABS	2250	1200	0,375	1,055	42,5	75	72,5
PLA	3100	1100	0,35	1,275	60	65	90
Epoxy	4000	1050	0,35	1,175	72,5	110	115
Nylon	2750	1000	0,4	1,14	80	80	115
Polyester	3000	1100	0,37	1,385	65	80	105
Vinyl Ester	3300	1200	0,36	1,135	80	110	135

Table 23: Appendix: Resin properties used for structural analysis

Fiber	E1 (MPa)	E2 (MPa)	Shear M. (MPa)	Poisson's Ratio	Density (g/cm^8)	Tensile S. (MPa)	Compressive S. (MPa)	Shear S. (MPa)
Glass E	72000	8000	30000	0,22	2,58	3400	1000	1200
Glass S	86000	9000	35000	0,23	2,49	4600	1600	1400
Kevlar	130000	5000	5000	0,36	1,44	3600	2000	2200
HS carbon	240000	15000	25000	0,2	1,8	4000	2500	3000
OK carbon	230000	15000	25000	0,2	1,75	3500	2000	2500
HM carbon	390000	15000	20000	0,2	1,9	2500	1800	2000

Table 24: Appendix: Fiber properties used for structural analysis

F Archive

The archive supports the outcomes and findings generated during the research process by providing the complete set of produced data. The repository includes analysis files and are divided into thematic folders for easy navigation. This resource is intended to provide full transparency and enable in-depth exploration of the data supporting the findings presented in the thesis.

Access the archive here:
https://drive.google.com/drive/folders/1D56bQ2Qt77PIOYtLHoyqnygHAgyF6IBv?usp=drive_link

For detailed instructions on navigating the archive and using the files, as well as the required software and licences, please refer to the readme.txt file within the archive.